

# Numerical analysis of Brazilian split test on concrete cylinder

Adam Wosatko, Andrzej Winnicki and Jerzy Pamin\*

Faculty of Civil Engineering, Cracow University of Technology, Warszawska 24  
31-155 Cracow, Poland

(Received June 23, 2009, Accepted June 22, 2010)

**Abstract.** The paper presents simulations of the Brazilian test using two numerical models. Both models are regularized in order to obtain results independent of discretization. The first one, called gradient damage, is refined by additional averaging equation which contains gradient terms and an internal length scale as localization limiter. In the second one, called viscoplastic consistency model, the yield function depends on the viscoplastic strain rate. In this model regularization properties are governed by the assumed strain rate. The two models are implemented in the FEAP finite element package and compared in this paper. Parameter studies of the split test are performed in order to point out the features of each model.

**Keywords:** Brazilian test; gradient damage; viscoplastic consistency; splitting; localization; concrete; FEM simulations.

---

## 1. Introduction

In the paper we analyze the behaviour of two regularized numerical models in the so-called Brazilian test. In laboratories this experimental test is used to establish the concrete tensile strength. It is one of basic fracture tests in the major concrete standards. The concrete cylinder or prism is subjected to a compressive vertical load through bearing strips in order to avoid multiple cracking and crushing, see Fig. 1. The compression between the loading platens induces a perpendicular tensile force in the middle of the specimen. Under the influence of compression primary and secondary cracks can form (Rocco *et al.* 1999, Rodriguez-Ferran and Huerta 2001) and splitting inside the specimen is observed. The splitting tensile strength  $f_t^s$  can be evaluated according to the formula, see e.g. in (Chen and Chang 1978, Rocco *et al.* 2001)

$$f_t^s = \frac{2P_{max}}{\pi BD} \quad (1)$$

where  $P_{max}$  is the maximum load recorded during the test,  $B$  and  $D$  are characteristic sizes of the specimen. In the case of a cylinder –  $B$  is the width and  $D$  is the diameter.

In the numerical simulation, according to the experiment, strain localization is expected in the vertical central zone of the specimen between load-transferring strips as is shown e.g. in (Feenstra 1993, Rodriguez-Ferran and Huerta 2001). The prismatic specimen was computed for example by

---

\* Corresponding author, Ph.D., E-mail: [jpamin@L5.pk.edu.pl](mailto:jpamin@L5.pk.edu.pl)

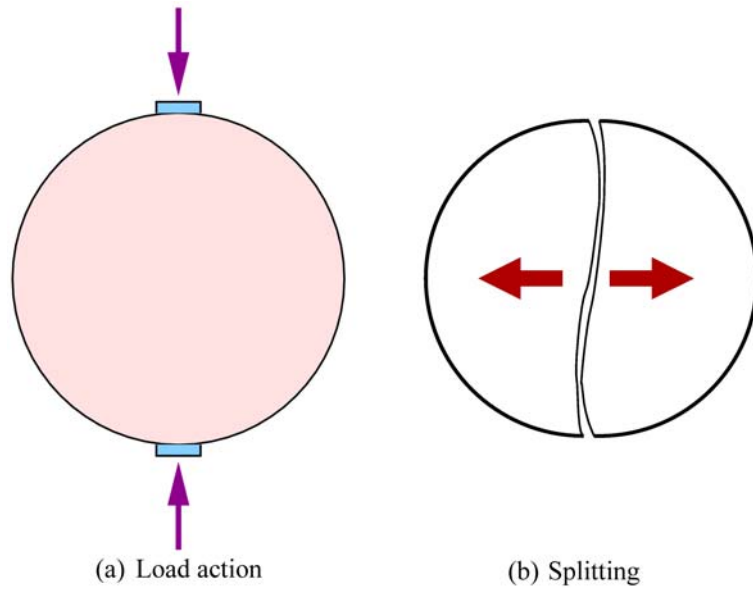


Fig. 1 Idea of Brazilian split test

Lopez *et al.* (2008). The cylinder specimen is simulated here in plane strain conditions, but plane stress (Winnicki *et al.* 2001) or 3D analyses (Ruiz *et al.* 2000) are also possible. We assume small strains and static loading.

The paper is organized as follows. Section 2 contains a compact description of the gradient enhancement for the scalar damage model (Peerlings *et al.* 1996). Apart from the nonlinear constitutive relation an additional averaging equation is enclosed in the system of equations, hence displacements and an averaged strain measure are interpolated. In Section 3 we summarize the derivation of the viscoplastic consistency model. This theory proposed by Wang (1997) for metals is developed here for concrete according to Winnicki (2007). It is assumed that the yield function can expand or shrink depending on the actual viscoplastic strain rate. The Burzyński-Hoffman surface in its isotropic form is selected as the yield surface and two internal variables can describe in a separate way hardening/softening behaviour in compression and tension. In Section 4 we set together the geometry and discretization of the Brazilian test, the general material data like Young's modulus and also the data for each model. The results of simulations are discussed in Section 5, in turn: for gradient damage in Subsection 5.1, for viscoplastic consistency in Subsection 5.2 and finally a comparison of these models is performed in Subsection 5.3. Conclusions are detailed in Section 6.

## 2. Gradient damage model

### 2.1 Constitutive relation

The simplest model of continuum damage mechanics which can describe elastic stiffness degradation in quasi-brittle materials is scalar damage. This means that one damage measure  $\omega$ , which grows monotonically from 0 to 1 (Kachanov 1958), is a function of damage history parameter  $\kappa^d$  and

depends on the deformation of a body. For a material without any defect (the lack of damage) the parameter  $\omega$  equals to 0. For a material with a complete loss of stiffness (total damage) we have  $\omega = 1$ .

Considering the damage evolution we distinguish the actual body with strains  $\boldsymbol{\varepsilon}$  and stresses  $\boldsymbol{\sigma}$  and its fictitious undamaged counterpart with stresses  $\hat{\boldsymbol{\sigma}}$  and strains  $\hat{\boldsymbol{\varepsilon}}$ . The fictitious counterpart represents the undamaged “skeleton” of the body, and the stresses  $\hat{\boldsymbol{\sigma}}$  acting on it are called effective. We adopt the postulate that the strains  $\boldsymbol{\varepsilon}$  observed in the actual body and in its undamaged representation  $\hat{\boldsymbol{\varepsilon}}$  are equal (Lemaitre 1971, Simo and Ju 1987). Then, the real stress tensor  $\boldsymbol{\sigma}$  and its effective counterpart  $\hat{\boldsymbol{\sigma}}$  are related by the above-mentioned parameter  $\omega$

$$\boldsymbol{\sigma} = (1 - \omega) \hat{\boldsymbol{\sigma}} \quad (2)$$

where

$$\hat{\boldsymbol{\sigma}} = \mathbf{E} : \boldsymbol{\varepsilon}^e \quad (3)$$

Here  $\mathbf{E}$  is the elastic stiffness operator. It is assumed here that the elastic strain tensor  $\boldsymbol{\varepsilon}^e$  is equal to the strain tensor  $\boldsymbol{\varepsilon}$  when the standard elasto-damage model is considered, but the model can easily be coupled with a plastic behaviour of the undamaged “skeleton”, cf. (de Borst *et al.* 1999). The so-called damage stress  $\boldsymbol{\sigma}^d$  which describes the change in the stress state due to damage can be defined as

$$\boldsymbol{\sigma}^d = \omega \mathbf{E} : \boldsymbol{\varepsilon} \quad (4)$$

so Eq. (2) can also be written as follows

$$\boldsymbol{\sigma} = \hat{\boldsymbol{\sigma}} - \boldsymbol{\sigma}^d \quad (5)$$

The strain equivalence is related with a loading function  $f^d$ , also called damage activation function, defined in the strain space

$$f^d(\boldsymbol{\varepsilon}, \kappa^d) = \tilde{\boldsymbol{\varepsilon}}(\boldsymbol{\varepsilon}) - \kappa^d = 0 \quad (6)$$

Here  $\tilde{\boldsymbol{\varepsilon}}$  is an equivalent strain measure. During the damage evolution the history parameter  $\kappa^d$  is equal to the largest value of  $\tilde{\boldsymbol{\varepsilon}}$  reached in the loading history. The activation of damage obeys the loading/unloading conditions written in the Kuhn-Tucker form

$$f^d \leq 0 \quad \dot{\kappa}^d \geq 0 \quad \dot{\kappa}^d f^d = 0 \quad (7)$$

The equivalent strain measure  $\tilde{\boldsymbol{\varepsilon}}$  can be defined in different ways. In this paper we employ the modified von Mises definition involving the first and second strain invariants,  $I_1^\varepsilon$  and  $J_2^\varepsilon$ , respectively, (de Vree *et al.* 1995)

$$\tilde{\boldsymbol{\varepsilon}} = \frac{k-1}{2k(1-2\nu)} I_1^\varepsilon + \frac{1}{2k\sqrt{\left(\frac{k-1}{1-2\nu} I_1^\varepsilon\right)^2 + \frac{12k}{(1+\nu)^2} J_2^\varepsilon}} \quad (8)$$

The loading functions for plane strain and plane stress conditions depending on Poisson's ratio  $\nu$  are put together in Fig. 2. The parameter  $k$  is the ratio of compressive and tensile strength  $f_c'$  and  $f_t'$ , respectively:

$$k = \frac{f_c'}{f_t'} \quad (9)$$

The elastic state envelopes for different values of  $k$  are depicted in Fig. 2(b).

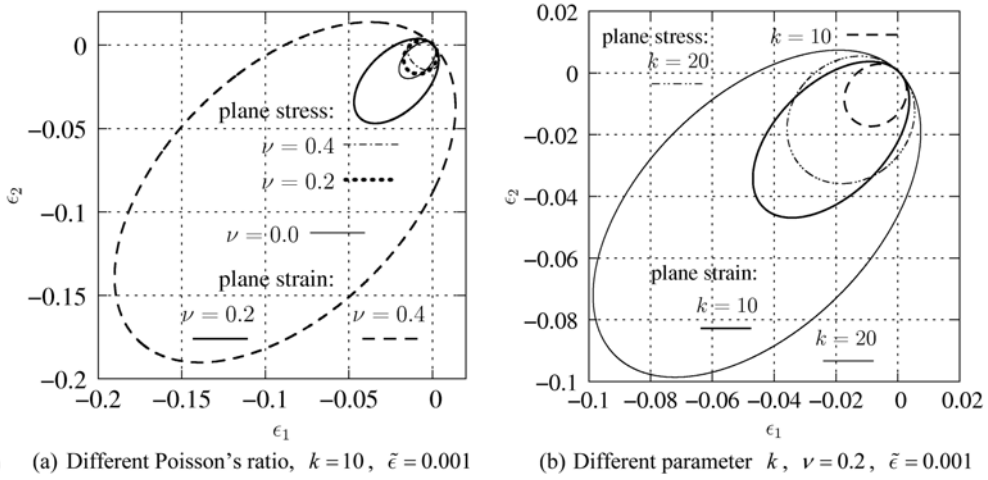


Fig. 2 Sensitivity of modified von Mises function in strain space to values of  $\nu$  and  $\kappa$

It is assumed that  $\kappa^d$  permanently grows from damage threshold  $\kappa_o$  to infinity and damage  $\omega$  asymptotically increases but never reaches 1. We define the damage growth function according to Mazars and Pijaudier-Cabot (1989) and Peerlings *et al.* (1998)

$$\omega(\kappa^d) = 1 - \frac{\kappa_o}{\kappa^d} (1 - \alpha + \alpha e^{-\eta(\kappa^d - \kappa_o)}) \quad (10)$$

The respective parameters  $\eta$  and  $\alpha$  are responsible for the rate of softening and residual stress which in one dimension tends to  $(1 - \alpha)E\kappa_o$ . The former parameter is thus connected with material ductility and related to concrete fracture energy  $G_f$ . The latter one prevents the complete loss of material stiffness and residual stresses remain only if  $\alpha < 1$ , which leads to a more stable numerical response.

If unloading is considered, irreversible strains are usually observed in concrete. In this case the motivation for coupling the damage model with plasticity is substantial. A combination of a plasticity theory formulated in the effective stress space with the above damage theory formulated in the strain space is described for instance by de Borst *et al.* (1999). In addition, the constitutive relations can incorporate a crack-closing projection operator which is important for cyclic loading and extensive stress redistributions (see e.g. Pamin *et al.* 2003).

## 2.2 Gradient enhancement and finite elements

Following Peerlings *et al.* (1996), the damage evolution in the gradient-enhanced model is governed by the following damage loading function

$$f^d(\boldsymbol{\varepsilon}, \kappa^d) = \bar{\varepsilon}(\tilde{\boldsymbol{\varepsilon}}(\boldsymbol{\varepsilon})) - \kappa^d = 0 \quad (11)$$

where the averaged (nonlocal) strain measure  $\bar{\varepsilon}$  satisfies the following differential equation

$$\bar{\varepsilon} - c \nabla^2 \bar{\varepsilon} = \tilde{\varepsilon} \quad (12)$$

The parameter  $c > 0$  has a unit of length squared and is related to an internal length scale  $l$  by

$c = (1/2)l^2$  (Askes *et al.* 2000). It is assumed here to be constant, although, with some modifications in the formulation, it can be made a function of  $\tilde{\varepsilon}$  or  $\bar{\varepsilon}$  (Geers 1997), which might be physically relevant.

Hereafter in this subsection Voigt's notation is used. We consider a certain domain  $B$ , occupied by the material body, with boundary  $\partial B$ . The weak form of equilibrium equations is the virtual work equation

$$\int_B \delta \boldsymbol{\varepsilon}^T \boldsymbol{\sigma} dV = \int_B \delta \mathbf{u}^T \mathbf{b} dV + \int_{\partial B} \delta \mathbf{u}^T \mathbf{t} dS \quad (13)$$

where the superscript  $T$  is the transpose symbol. In the above equation  $\mathbf{b}$  is the body force vector and  $\mathbf{t}$  is the traction vector. The weak form of Eq. (12) is derived as follows. The variation of the averaged strain measure  $\delta \bar{\varepsilon}$ , Green's formula and the natural boundary condition  $(\nabla \bar{\varepsilon})^T \mathbf{v} = 0$  are introduced to obtain

$$\int_B \delta \bar{\varepsilon} \bar{\varepsilon} dV = \int_B (\nabla \delta \bar{\varepsilon})^T c \nabla \bar{\varepsilon} dV = \int_B \delta \bar{\varepsilon} \tilde{\varepsilon} dV \quad (14)$$

In the ensuing two-field formulation averaged strain measure  $\bar{\varepsilon}$  must be discretized in addition to displacements  $\mathbf{u}$ . These primary fields are interpolated in the following way

$$\mathbf{u} = \mathbf{N} \mathbf{a} \quad \text{and} \quad \bar{\varepsilon} = \mathbf{h}^T \mathbf{e} \quad (15)$$

where  $\mathbf{N}$  and  $\mathbf{h}$  contain suitable shape functions. From the above interpolations the secondary fields  $\boldsymbol{\varepsilon}$  and  $\nabla \bar{\varepsilon}$  are computed

$$\boldsymbol{\varepsilon} = \mathbf{B} \mathbf{a} \quad \text{and} \quad \nabla \bar{\varepsilon} = \mathbf{g}^T \mathbf{e} \quad (16)$$

where  $\mathbf{B} = \mathbf{L} \mathbf{N}$ ,  $\mathbf{g}^T = \nabla \mathbf{h}^T$ ,  $\mathbf{L}$  is a differential operator matrix. After discretization, applied also for variations  $\delta \mathbf{u}$  and  $\delta \bar{\varepsilon}$ , Eqs. (13) and (14) must hold for any admissible  $\delta \mathbf{a}$  and  $\delta \mathbf{e}$ .

The boundary value problem is linearized, hence at nodal points the increments of the primary fields from iteration  $i$  to iteration  $i + 1$  are introduced according to the following decomposition

$$\mathbf{a}^{i+1} = \mathbf{a}^i + \Delta \mathbf{a} \quad \text{and} \quad \mathbf{e}^{i+1} = \mathbf{e}^i + \Delta \mathbf{e} \quad (17)$$

Analogically, at integration points we decompose secondary fields, for example the stress

$$\boldsymbol{\sigma}^{(i+1)} = \boldsymbol{\sigma}^{(i)} + \Delta \boldsymbol{\sigma} \quad (18)$$

Hence the constitutive relation is written in its incremental version

$$\Delta \boldsymbol{\sigma} = (1 - \omega^i) \mathbf{E} \Delta \boldsymbol{\varepsilon} - \Delta \omega \hat{\boldsymbol{\sigma}}^i \quad (19)$$

The increment of damage  $\Delta \omega$  depends on the increment of averaged strain  $\Delta \bar{\varepsilon}$

$$\Delta \omega = \left[ \frac{\partial \omega}{\partial \kappa^d} \right]^i \left[ \frac{\partial \kappa^d}{\partial \bar{\varepsilon}} \right]^i \Delta \bar{\varepsilon} = \mathcal{G}^i \mathbf{h}^T \Delta \mathbf{e} \quad (20)$$

In the averaging equation the increment of equivalent strain measure  $\Delta \bar{\varepsilon}$  is computed from the interpolated displacement increment  $\Delta \mathbf{a}$

$$\Delta \tilde{\varepsilon} = \left[ \frac{d \tilde{\varepsilon}}{d \boldsymbol{\varepsilon}} \right]^i \Delta \boldsymbol{\varepsilon} = [\mathbf{v}^T]^i \mathbf{B} \Delta \mathbf{a} \quad (21)$$

Finally, we rewrite Eqs. (13) and (14) in a matrix form, so that the gradient damage formulation can

be written as the coupled matrix problem

$$\begin{bmatrix} \mathbf{K}_{aa} & \mathbf{K}_{ae} \\ \mathbf{K}_{ea} & \mathbf{K}_{ee} \end{bmatrix} \begin{bmatrix} \Delta \mathbf{a} \\ \Delta \mathbf{e} \end{bmatrix} = \begin{bmatrix} \mathbf{f}_{ext}^{i+1} - \mathbf{f}_{int}^i \\ \mathbf{f}_\varepsilon^i - \mathbf{f}_e^i \end{bmatrix} \quad (22)$$

The submatrices and vectors in Eq. (22) are like in the formulation presented by Peerlings *et al.* (1996)

$$\mathbf{K}_{aa} = \int_B \mathbf{B}^T (1 - \omega^i) \mathbf{E} \mathbf{B} dV \quad \text{and} \quad \mathbf{K}_{ae} = - \int_B \mathcal{G}^i \mathbf{B}^T \hat{\boldsymbol{\sigma}}^i \mathbf{h}^T dV \quad (23)$$

$$\mathbf{K}_{ea} = - \int_B \mathbf{h} [\mathbf{v}^T]^i \mathbf{B} dV \quad \text{and} \quad \mathbf{K}_{ee} = \int_B (\mathbf{h} \mathbf{h}^T + c \mathbf{g} \mathbf{g}^T) dV \quad (24)$$

$$\mathbf{f}_{ext}^{i+1} = \int_B \mathbf{N}^T \mathbf{b}^{i+1} dV + \int_{\partial B} \mathbf{N}^T \mathbf{t}^{i+1} dS \quad \text{and} \quad \mathbf{f}_{int}^i = \int_B \mathbf{B}^T \boldsymbol{\sigma}^i dV \quad (25)$$

$$\mathbf{f}_\varepsilon^i = \int_B \mathbf{h} \tilde{\boldsymbol{\varepsilon}}^i dV \quad \text{and} \quad \mathbf{f}_e^i = \mathbf{K}_{ee} \mathbf{e}^i \quad (26)$$

In the absence of damage growth  $\mathbf{K}_{ae} = \mathbf{0}$  and the equilibrium equations are uncoupled from the averaging equation.

We have implemented the finite elements in the FEAP package (Taylor 2001) using three variants of  $C^0$ -continuous interpolation, which is sufficient. In the first option elements with analogical linear interpolation (lin/lin) of both displacements  $\mathbf{u}$  and averaged strain  $\bar{\boldsymbol{\varepsilon}}$  are employed (elements called Q4/4). In the second option quadratic interpolation of the displacements and linear of the averaged strain is assumed (quad/lin), hence a different number of degrees of freedom at the corner and midside nodes is required (elements Q8/4). For the last group of elements quadratic interpolation (quad/quad) of both fundamental unknowns is introduced (elements Q8/8).

### 3. Burzyński-Hoffman viscoplasticity

The second employed model for concrete is developed within the viscoplasticity theory and follows the idea proposed by Wang (1997) for metals, named “the consistency model”. It was shown that the consistency model with constant viscoplastic modulus coincides with the model of Perzyna (1966) in the case of the simplest form of the “over-stress” function (Winnicki 2001). A similar approach was independently proposed by Kleiber (1998) and later developed by Heeres *et al.* (2002).

In the considered model the yield function can expand or shrink depending on the actual viscoplastic strain rate. The stress state is forced to remain on the yield surface and the consistency condition is invoked. There is no need for an additional equation defining a viscoplastic multiplier. Therefore, this approach is very close to the classical rate independent plasticity. The established numerical algorithms like the closest point projection or the cutting plane algorithm (Simo and Hughes 1997) can easily be adapted.

The Burzyński-Hoffman surface in its isotropic form is selected, since it has been successfully employed in the analysis of concrete structures (Bićanić *et al.* 1994, Pearce 1993). This yield surface is of the form (cf. also Życzkowski 1981)

$$f^{vp} = \frac{3}{2} \mathbf{s} : \mathbf{s} + \text{tr} \boldsymbol{\sigma} (f_c - f_t) - f_c f_t = 0 \quad (27)$$

where  $\mathbf{s}$  is the deviatoric stress tensor.

It is assumed that two internal variables  $\kappa_c$  and  $\kappa_t$  exist which are both functions of the equivalent viscoplastic strain. They describe in a separate way hardening/softening behaviour in compression and tension, respectively. In addition, two more internal variables  $\eta_c$  and  $\eta_t$  determine the increase/decrease of compressive and tensile strengths due to the actual rate of the equivalent viscoplastic strain. Thus, the actual compressive and tensile strengths are

$$f_c = f_c(\kappa_c, \eta_c) \quad \text{and} \quad f_t = f_t(\kappa_t, \eta_t) \quad (28)$$

The rates of the internal variables depend on the current stress and the rates of internal variables  $\kappa$  and  $\eta$

$$\dot{\kappa}_c = g_c(\boldsymbol{\sigma}) \dot{\kappa} \quad \text{and} \quad \dot{\kappa}_t = g_t(\boldsymbol{\sigma}) \dot{\kappa} \quad (29)$$

$$\dot{\eta}_c = g_c(\boldsymbol{\sigma}) \dot{\eta} \quad \text{and} \quad \dot{\eta}_t = g_t(\boldsymbol{\sigma}) \dot{\eta} \quad (30)$$

In the above equations  $g_c$  and  $g_t$  are scalar functions of stress accounting for independent processes of damage in compression and tension. In turn,  $\dot{\kappa}$  is defined as an equivalent viscoplastic strain (in the rate form) assuming work hardening, and in a similar way  $\dot{\eta}$  depends on first derivatives of the viscoplastic strain (i.e. its rate is a function of second derivatives)

$$\dot{\kappa} = \frac{\boldsymbol{\sigma} : \dot{\boldsymbol{\epsilon}}^{vp}}{\sqrt{\frac{3}{2} \mathbf{s} : \mathbf{s}}} \quad \text{and} \quad \dot{\eta} = \frac{\boldsymbol{\sigma} : \dot{\boldsymbol{\epsilon}}^{vp}}{\sqrt{\frac{3}{2} \mathbf{s} : \mathbf{s}}} \quad (31)$$

It should be noted that in the course of loading the yield surface can change its shape due to the separate hardening/softening processes of the compressive and tensile strength, although the surface remains convex at all times (see Fig. 3).

The strain rate is decomposed into its elastic and viscoplastic parts

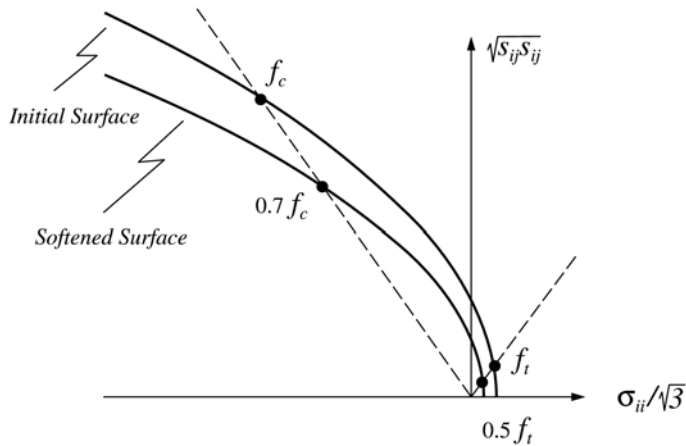


Fig. 3 The initial and softened yield surface ( $f_c/f_t = 10$ )

$$\dot{\boldsymbol{\varepsilon}} = \dot{\boldsymbol{\varepsilon}}^e + \dot{\boldsymbol{\varepsilon}}^{vp} \quad (32)$$

and the generalized Hooke's law is valid for the elastic part:

$$\dot{\boldsymbol{\sigma}} = \mathbf{E} : \dot{\boldsymbol{\varepsilon}}^e \quad (33)$$

The viscoplastic flow is defined similarly to the classical associated plasticity and to the Perzyna model

$$\dot{\boldsymbol{\varepsilon}}^{vp} = \dot{\lambda} \mathbf{m} \quad (34)$$

where the plastic flow tensor

$$\mathbf{m} = \frac{\partial f^{vp}}{\partial \boldsymbol{\sigma}} = 3\mathbf{s} + \mathbf{I}(f_c - f_t) \quad (35)$$

where  $\mathbf{I}$  is the unit tensor.

The difference between this model and the classical associated plasticity lies in the definition of the yield surface which depends not only on the internal parameter  $\kappa$  but also on the additional one  $\eta$ . Since the total value of the latter depends on the first derivatives of viscoplastic strains, the yield surface is rate dependent and can change its size and shape according to the value of the viscoplastic strain rate - i.e. expands for higher rates and shrinks for lower rates. As a result, this model can correctly predict basic viscoplastic phenomena like creep and relaxation.

The functions  $g_c$  and  $g_t$  from Eqs. (29)-(30) are selected according to the experimental evidence taking into account the influence of the damage process in compression on the concrete strength in tension and, vice versa, the influence of the damage process in tension on the concrete strength in compression. Hence, two very simple options are possible:

- In the first approach (called further "isotropic") it is assumed that damage is an isotropic phenomenon

$$g_c = g_t = 1 \quad (36)$$

- In the second approach (called further "nonisotropic") for a loading process with dominant compressive stress  $g_c = 1$  and  $g_t = 0$  (i.e. the value of  $f_t$  is not affected by the process) and for a loading process with dominant tensile stress  $g_c = 0$  and  $g_t = 1$ . The following relation is introduced

$$g_c + g_t = 1 \quad (37)$$

The details of this idea can be found in (Winnicki, 2007).

The dependence of  $f_c$  on  $\kappa_c$  and  $\eta_c$  is formulated in a general way as

$$f_c = f_c' H_c(\kappa_c) S_c(\eta_c) \quad (38)$$

where  $f_c'$  is the initial compressive strength. Functions  $H_c$  and  $S_c$  are specified as piece-wise linear. Example functions, based on experimental data from Kupfer (1973) and Suaris and Shah (1985), are presented in Figs. 4(a) and 4(c), respectively. Similarly, the actual tensile strength is computed as

$$f_t = f_t' H_t(\kappa_t) S_t(\eta_t) \quad (39)$$

Again, the plots of functions  $H_t$  and  $S_t$ , based on experimental data performed by Reinhardt (1984) and Suaris and Shah (1985), are given in Figs. 4(b) and 4(d), respectively. Please, note that function  $H_c$  accounts for both hardening and softening behaviour in uniaxial compression. Therefore, at the beginning

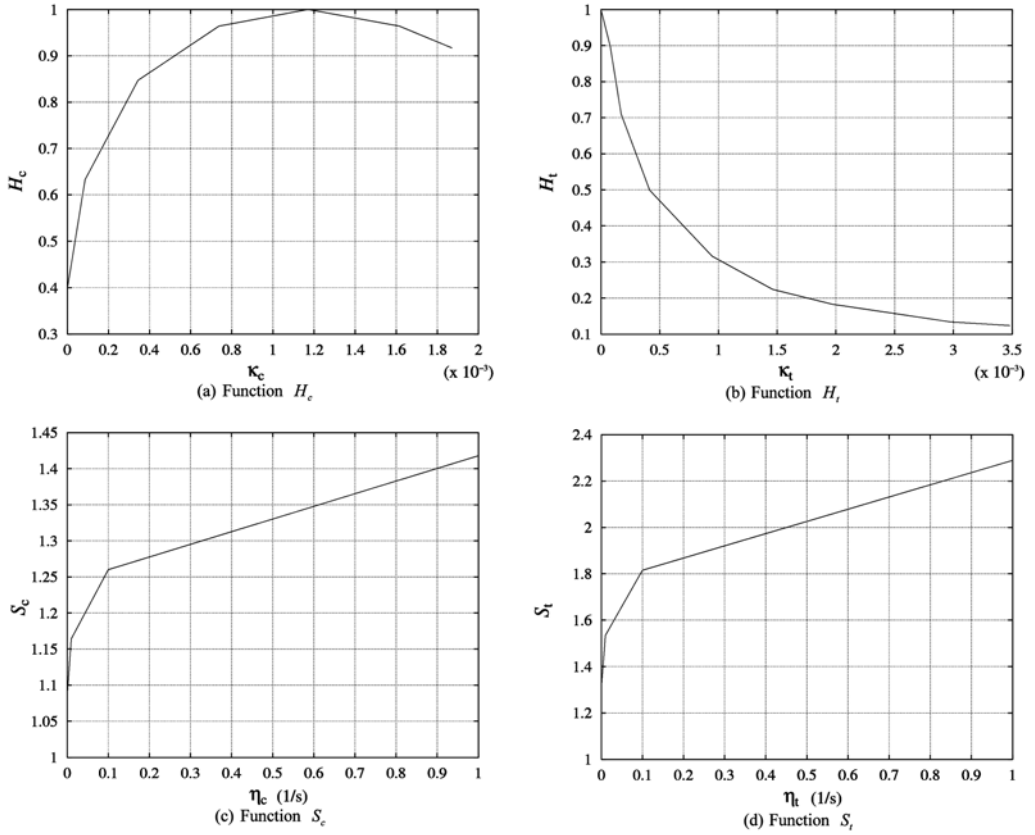


Fig. 4 Exemplary plastic modulus functions

of the loading process  $H_c < 1$  is assumed causing the initial yield surface (elastic locus) to be contained inside the bounding surface given by Eq. (27) with  $H_c = H_t = S_c = S_t = 1$ . In other words, in compression the yield surface primarily expands and then shrinks whereas in tension it only shrinks.

In order to establish the viscoplastic multiplier  $\lambda$  the consistency equation is used, which takes a form

$$\mathbf{m}:\dot{\boldsymbol{\sigma}} + \frac{\partial f^{vp}}{\partial \kappa_c} \dot{\kappa}_c + \frac{\partial f^{vp}}{\partial \eta_c} \dot{\eta}_c + \frac{\partial f^{vp}}{\partial \kappa_t} \dot{\kappa}_t + \frac{\partial f^{vp}}{\partial \eta_t} \dot{\eta}_t = 0 \quad (40)$$

Using Eqs. (29), (30), (31), (34) derivatives  $\dot{\kappa}_c$ ,  $\dot{\kappa}_t$ ,  $\dot{\eta}_c$ ,  $\dot{\eta}_t$  can be expressed as

$$\dot{\kappa}_c = g_c g \dot{\lambda} \quad \dot{\kappa}_t = g_t g \dot{\lambda} \quad \dot{\eta}_c = g_c g \ddot{\lambda} \quad \dot{\eta}_t = g_t g \ddot{\lambda} \quad (41)$$

Where  $g$  is equal to

$$g = \frac{\boldsymbol{\sigma}:\mathbf{m}}{\sqrt{\frac{3}{2}}\mathbf{s}:\mathbf{s}} \quad (42)$$

Using the above relationships the consistency equation can be worked out in a form depending on  $\dot{\lambda}$  and  $\ddot{\lambda}$

$$\mathbf{m}:\dot{\boldsymbol{\sigma}} - h\dot{\lambda} - s\ddot{\lambda} = 0 \quad (43)$$

where  $h$  is the classical generalized plastic modulus and  $s$  is the generalized viscoplastic modulus. Due to the last term the consistency equation is no longer an algebraic equation for the viscoplastic multiplier, but a differential equation of the first order, to be solved for an appropriate initial condition.

The detailed forms of the generalized plastic and viscoplastic moduli are

$$h = a_c S_c h_c + a_t S_t h_t \quad \text{and} \quad s = a_c s_c H_c + a_t s_t H_t \quad (44)$$

where

$$h_c = \frac{dH_c}{d\kappa_c} \quad h_t = \frac{dH_t}{d\kappa_t} \quad s_c = \frac{dS_c}{d\eta_c} \quad s_t = \frac{dS_t}{d\eta_t} \quad (45)$$

In turn, coefficients  $a_c$  and  $a_t$  are

$$a_c = f_c'(f_t - \text{tr} \boldsymbol{\sigma}) g_c g \quad \text{and} \quad a_t = f_t'(f_c + \text{tr} \boldsymbol{\sigma}) g_c g \quad (46)$$

In the case when the functions  $S_c$  and  $S_t$  are constant, their derivatives vanish and Eq. (43) reduces to the form known from the classical rate independent plasticity.

The fracture energies in uniaxial tension and compression for the case  $S_t = S_c \equiv 1$  can be computed as

$$g_{ft} = \int_{\varepsilon_{11,t,0}^{vp}}^{\infty} \sigma_{11} d\varepsilon_{11}^{vp} = \bar{f}_t \int_{\varepsilon_{11,t,0}^{vp}}^{\infty} H_t(\kappa_t) d\varepsilon_{11}^{vp} \quad (47)$$

and

$$g_{fc} = \int_{\varepsilon_{11,c,0}^{vp}}^{\infty} \sigma_{11} d\varepsilon_{11}^{vp} = \bar{f}_c \int_{\varepsilon_{11,c,0}^{vp}}^{\infty} H_c(\kappa_c) d\varepsilon_{11}^{vp} \quad (48)$$

where  $\varepsilon_{11,t,0}^{vp}$  and  $\varepsilon_{11,c,0}^{vp}$  are the values of viscoplastic strain  $\varepsilon_{11}^{vp}$  in tension and compression associated with the maximum of functions  $H_t$  and  $H_c$ , respectively. Fracture energies  $g_{ft}$  and  $g_{fc}$  defined by Eqs. (47)-(48) are computed from the stress – viscoplastic strain curves and not from the stress – displacement curves in the postcritical range (hence, they have dimensions Pa and not N/m). In order to get fracture energies  $G_{ft}$  and  $G_{fc}$  which are the actual material properties (fib 1999, van Mier 1984, Vonk 1992) the respective fracture energies at the material point have to be multiplied by the width of the localization zone. For the case  $S_t = S_c \equiv 1$ , when the presented model is not a localisation limiter, the width of the localisation zone usually coincides with one row of finite elements. However, when viscous effects are active the width of localisation zone becomes larger and can only be estimated a posteriori. Therefore, in this model a direct relationship between  $g_{ft}$  and  $G_{ft}$  (or between  $g_{fc}$  and  $G_{fc}$ ) does not exist.

In the case of statics the finite element algorithm for the Burzyński-Hoffman viscoplastic model is similar to the classical rate-independent plasticity and only the weak form of equilibrium equations is discretized, see Eq. (13).

#### 4. Specification of numerical model

The geometry of the Brazilian tests is based on papers (Feenstra 1993, Winnicki *et al.* 2001). Due to double symmetry only a quarter of the domain (with radius equal to 40 mm) is considered. The general material data are presented in Table 1.

For gradient damage the load is applied to the specimen indirectly via a stiff platen (width -

Table 1 General material data

Specimen:	Nonlinear
Young's modulus:	$E_c = 37700$ MPa
Poisson's ratio:	$\nu = 0.15$
Material model:	Gradient damage
or	Viscoplastic consistency
Platen:	Elastic
Young's modulus:	$E_s = 10 E_c$
Poisson's ratio:	$\nu = 0.15$

Table 2 Gradient damage – basic model data

Equivalent strain measure:	Modified von Mises definition, $k = 10$
Damage growth function:	Exponential softening, $\alpha = 0.99$ , $\eta = 600$
Fracture energy:	$G_f = 0.075$ N/mm
Internal length scale:	$l = 6$ mm, i.e. $c = 180$ mm <sup>2</sup>
Threshold:	$\kappa_o = 7.9576 \times 10^{-5}$

Table 3 Discretizations used in simulations

Coarse meshes			
Name	C12 (Fig. 5(a))	C20	C24
Used FE	Q4/4	Q8/4	Q8/8
Interpolation	lin/lin	quad/lin	quad/quad
Dofs/element	12	20	24
Nodes/sym.edge	17	17	17
Elms/sym.edge	16	8	8
Medium meshes			
Name	M12	M20	M24
Used Fe	Q4/4	Q8/4	Q8/8
Interpolation	lin/lin	quad/lin	quad/quad
Dofs/element	12	20	24
Nodes/sym.edge	33	33	33
Elms/sym.edge	32	16	16
Fine meshes			
Name	F12	F20 (Fig. 5(c))	F24 (Fig. 5(c))
Used FE	Q4/4	Q8/4	Q8/8
Interpolation	lin/lin	quad/lin	quad/quad
Dofs/element	12	20	24
Nodes/sym.edge	65	65	65
Elms/sym.edge	64	32	32

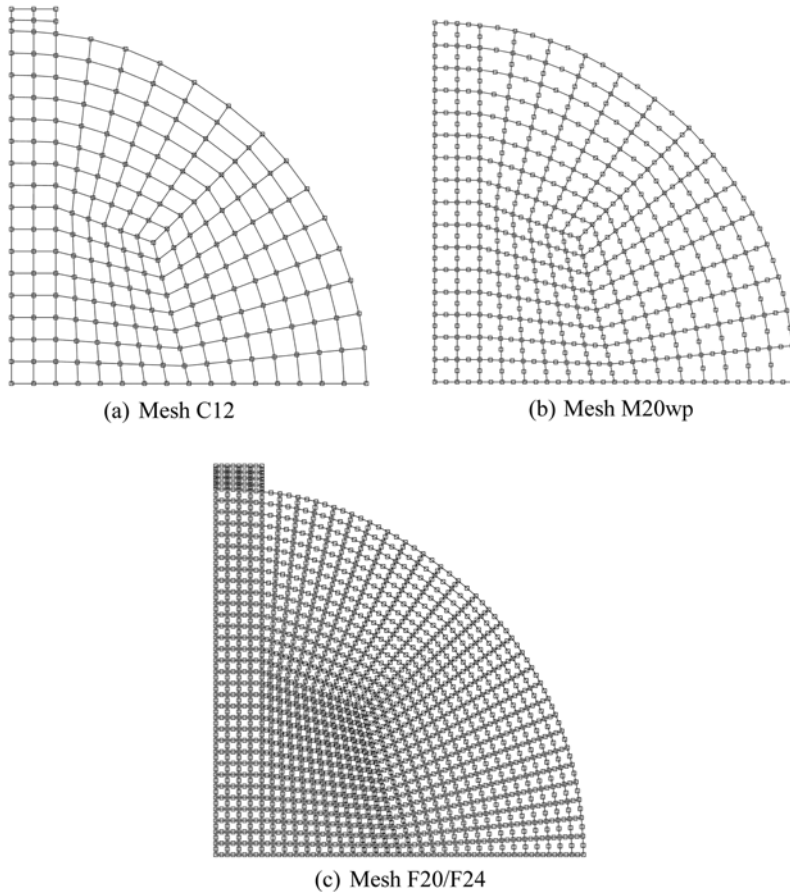


Fig. 5 Exemplary meshes

5 mm, height - 2.5 mm). The basic data for this model are in Table 2. The platen is perfectly connected with the specimen. The load acts downwards at the top of the platen. The discretizations applied in computations for gradient damage are listed in Table 3. Selected meshes are shown in Fig. 5. The influence of mesh refinement is discussed in the next section. We also examine the influence of internal length  $l$  and ductility parameter  $\eta$ . To compare, in Subsection 5.3, direct loading without the platen is considered, see mesh M20wp in Fig. 5(b). In this case the load acts downwards at the edge part equivalent to the platen.

Because of a snapback response the test is computed using the arc length method. In the calculations selective integration is applied for lin/lin interpolation (FE Q4/4) and  $2 \times 2$  integration for the remaining elements.

Apart from general data given in Table 1, input parameters for the viscoplastic consistency model are shown in Table 4. In Fig. 6 the piecewise linearized forms of functions  $H_c$ ,  $H_t$ ,  $S_c$  and  $S_t$  are specified in order to set the relation between tension and compression during the loading process. For this model we focus our analysis on the investigation of the influence of the material parameters, so computations are performed using mainly the coarse mesh of four-noded elements (corresponding to mesh C12). The medium mesh with eight-noded elements (like M20) is applied only in the comparison in Subsection 5.3. The specimen is considered with or without the platen. In

Table 4 Viscoplastic consistency – basic model data in specimen

Equivalent viscoplastic strain:	Work hardening, Eq. (31)
Initial tensile strength:	$f_c' = 3$ MPa
Initial compressive strength:	$f_c' = 30$ MPa
Material curves:	Fig. 6

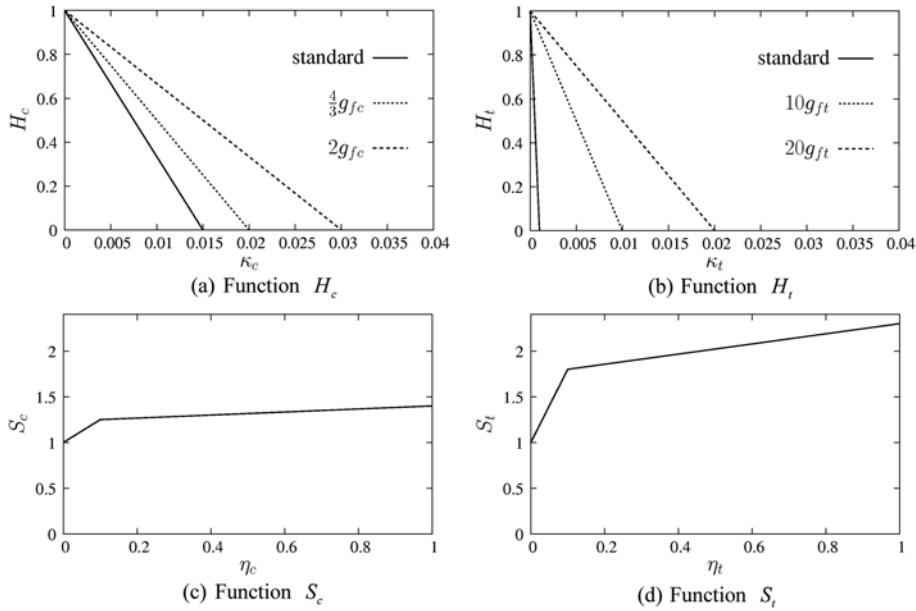


Fig. 6 Material functions for Burzyński-Hoffman viscoplasticity

Subsection 5.2, we first describe results which depend on the strain rate for the “isotropic” and “nonisotropic” version of the model. A linear softening character of  $H_c$  and  $H_t$  is assumed, which is called “standard” in Figs. 6(a) and 6(b). We take into account functions  $S_c$  and  $S_t$  shown in Fig. 6(c) and Fig. 6(d), respectively. Next, we assume the “isotropic” model,  $S_t = S_c \equiv 1$ , and analyze the response of the modelled specimen for different curves  $H_c$ , where the local fracture energies can be calculated according to Eq. (48) and is equal to either  $g_{fc} = 225.0$  kPa (standard case),  $(4/3)g_{fc} = 300.0$  kPa or  $2g_{fc} = 450.0$  kPa. Together with these results we also show an analogical analysis for different curves  $H_t$ , where from Eq. (47) the following local fracture energies can be computed:  $g_{ft} = 1.50$  kPa (standard case),  $10g_{ft} = 15.0$  kPa and  $20g_{ft} = 30.0$  kPa. In Subsection 5.3 we confront the results for this model in its “isotropic” version with those for gradient damage, assuming standard  $H_c$ ,  $H_t$  and  $S_t = S_c \equiv 1$ .

## 5. Results of simulations

### 5.1 Gradient damage model

In the simulations the vertical displacement at the top of the platen on the symmetry axis is measured, which grows with the applied loading. In Fig. 7 load-displacement diagrams for the used

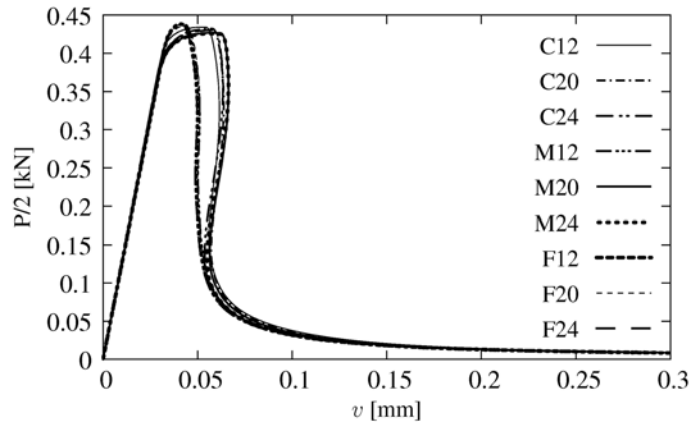


Fig. 7 Load-displacement diagrams for gradient damage – summary of used meshes

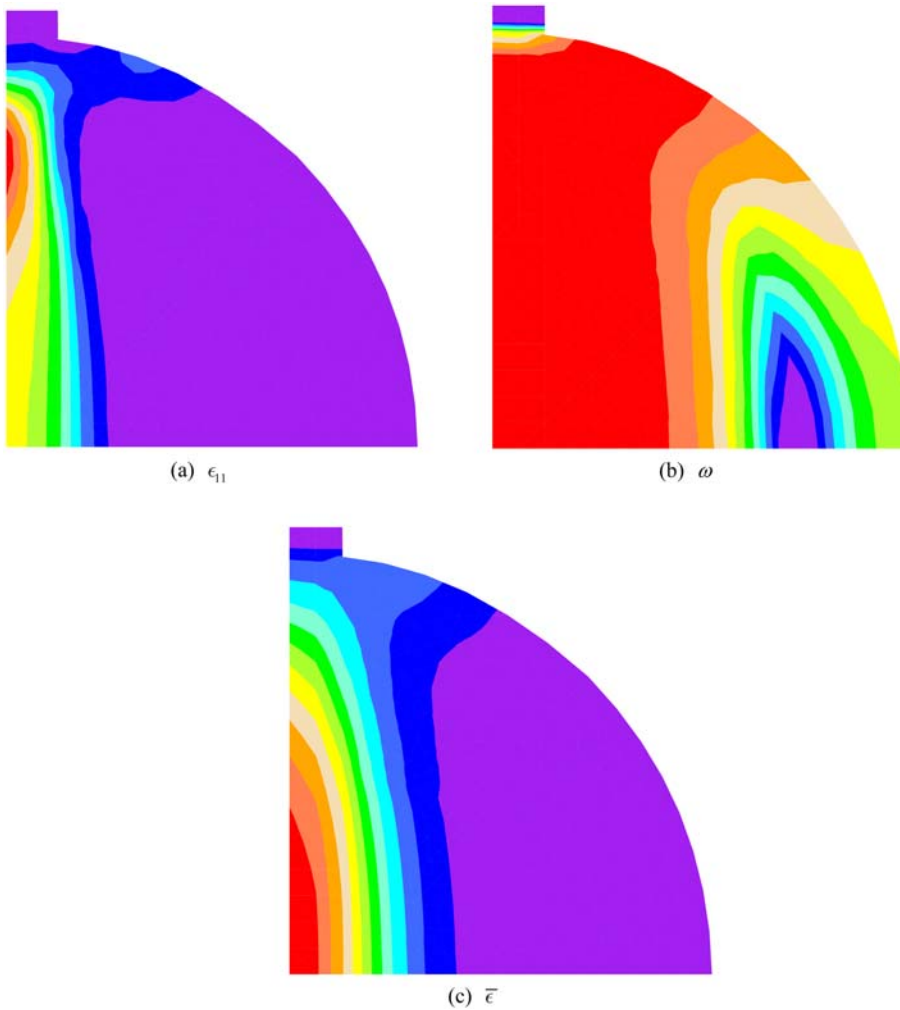


Fig. 8 Gradient damage – contour plots for mesh C12

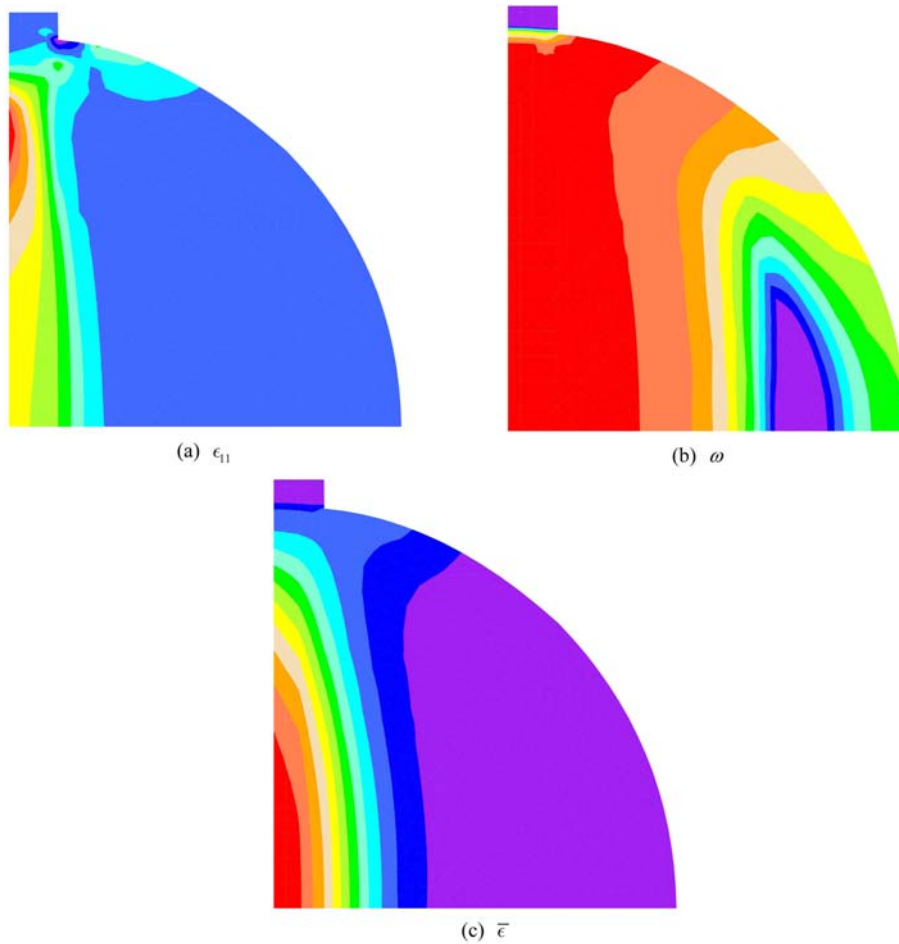


Fig. 9 Gradient damage – contour plots for mesh M20

meshes are presented. We observe a snapback response which is connected with the splitting process. In Fig. 7 two groups of diagrams are plotted. One group shows a sharper drop after a longer peak phase. It is for the computations performed with all coarse meshes, and medium meshes M20 or M24 (see Table 3). The second group of diagrams for all fine meshes and medium mesh M12 show the response with a more distinct peak and the snapback is less pronounced. An explanation why the solution for mesh M12 belongs to the second group can be found if we compare the mesh density and especially integration point density for the meshes. In this respect the refinement for mesh M12 is similar to meshes F20 and F24. Hence, an improvement of the approximation only slightly influences the loading path. In the final stage, the loading paths converge to the same residual load level.

The contour plots in Figs. 8-10 show the mesh independence of the results. We can notice the failure mode associated with primary crack formation (Rocco *et al.* 1999, Rodriguez-Ferran and Huerta 2001), i.e. a crack appears under the loading platen along the vertical symmetry axis. All the plots are depicted for the final points of the loading paths. Apart from the splitting we observe a concentration of strains in the area under the platen (see contour plots of the horizontal normal

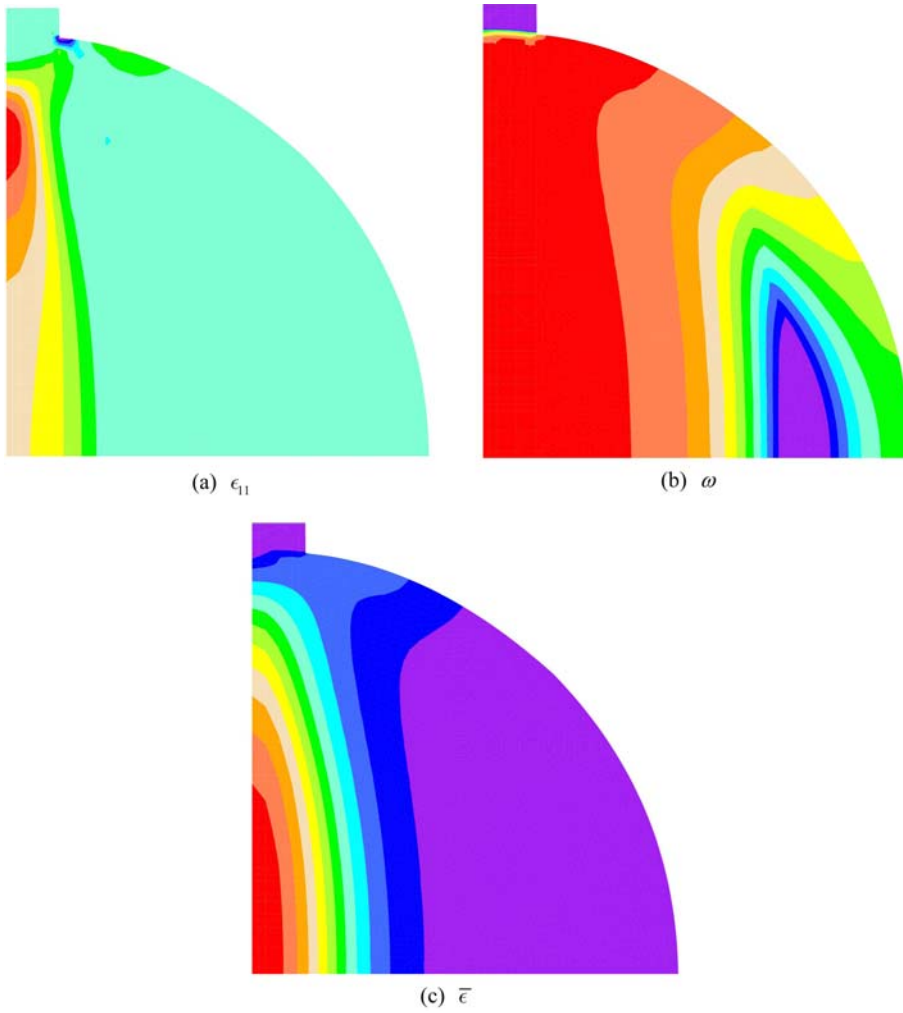


Fig. 10 Gradient damage – contour plots for mesh F24

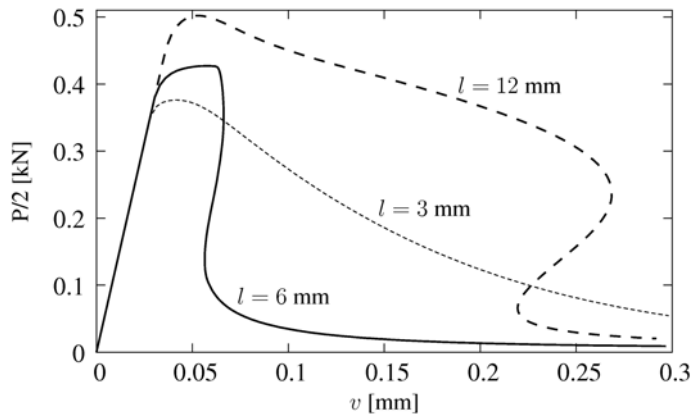


Fig. 11 Gradient damage, influence of internal length scale, diagrams

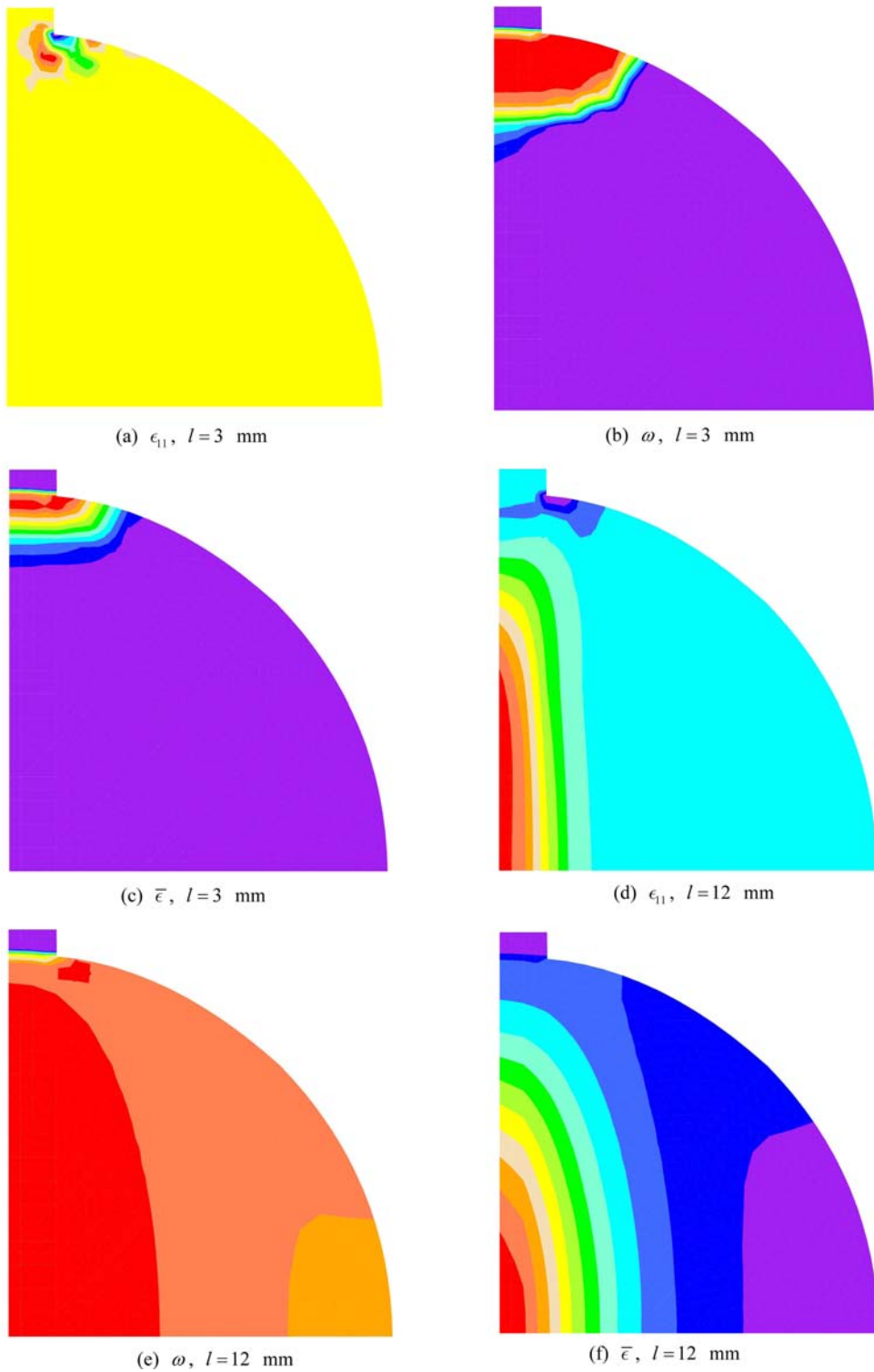


Fig. 12 Gradient damage, influence of internal length scale, contour plots

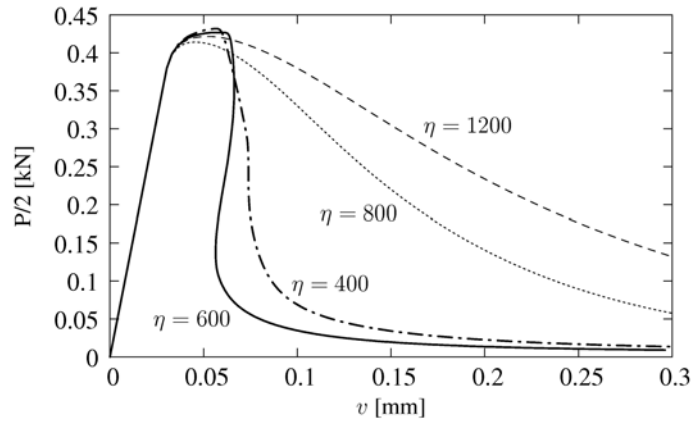


Fig. 13 Gradient damage, influence of ductility parameter, diagrams

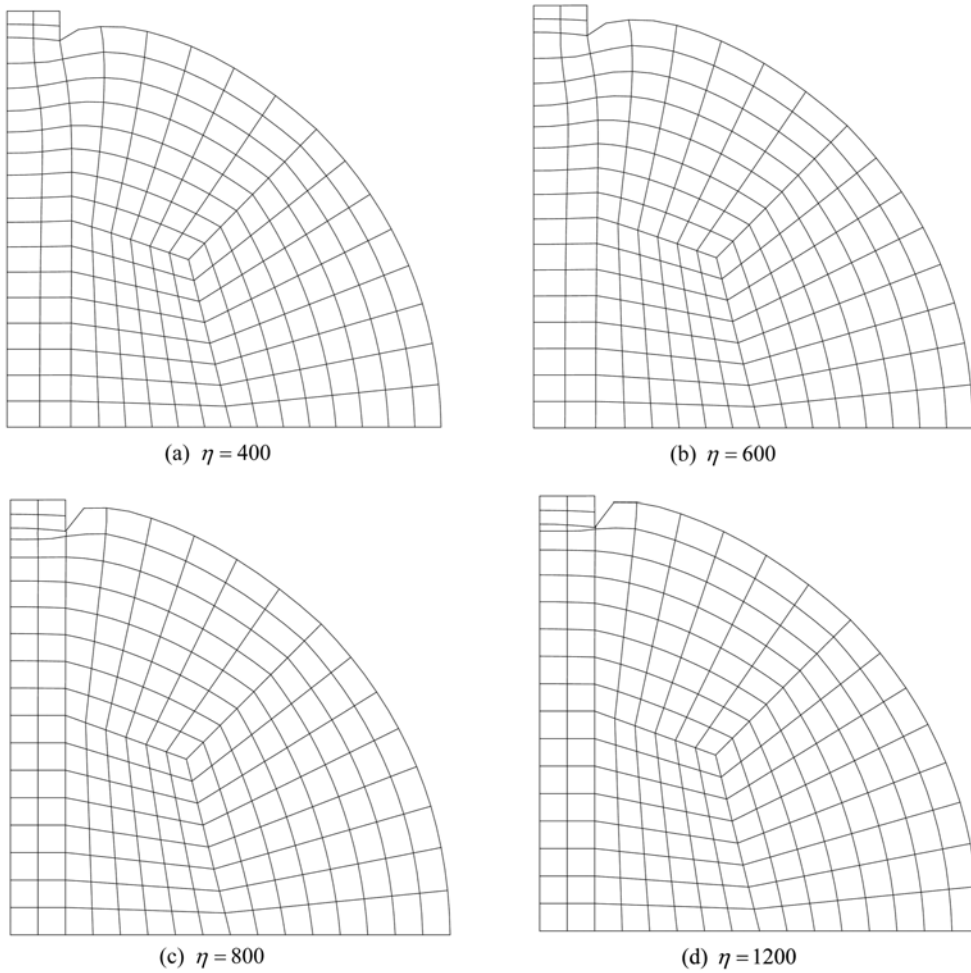


Fig. 14 Gradient damage, influence of ductility parameter, deformations

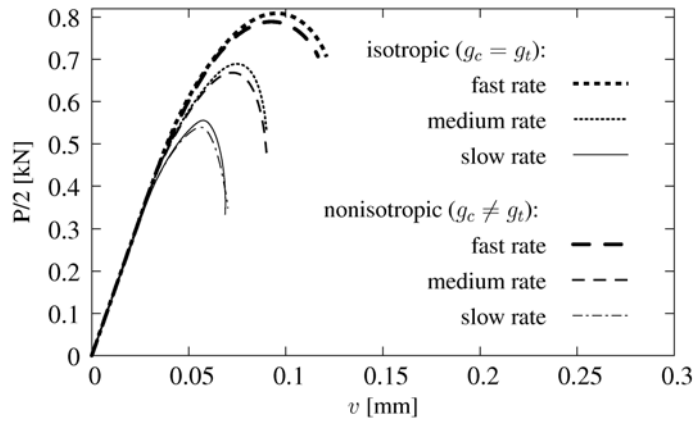


Fig. 15 Viscoplastic consistency, different load rates and relations of functions  $g_c$ - $g_t$ , diagrams

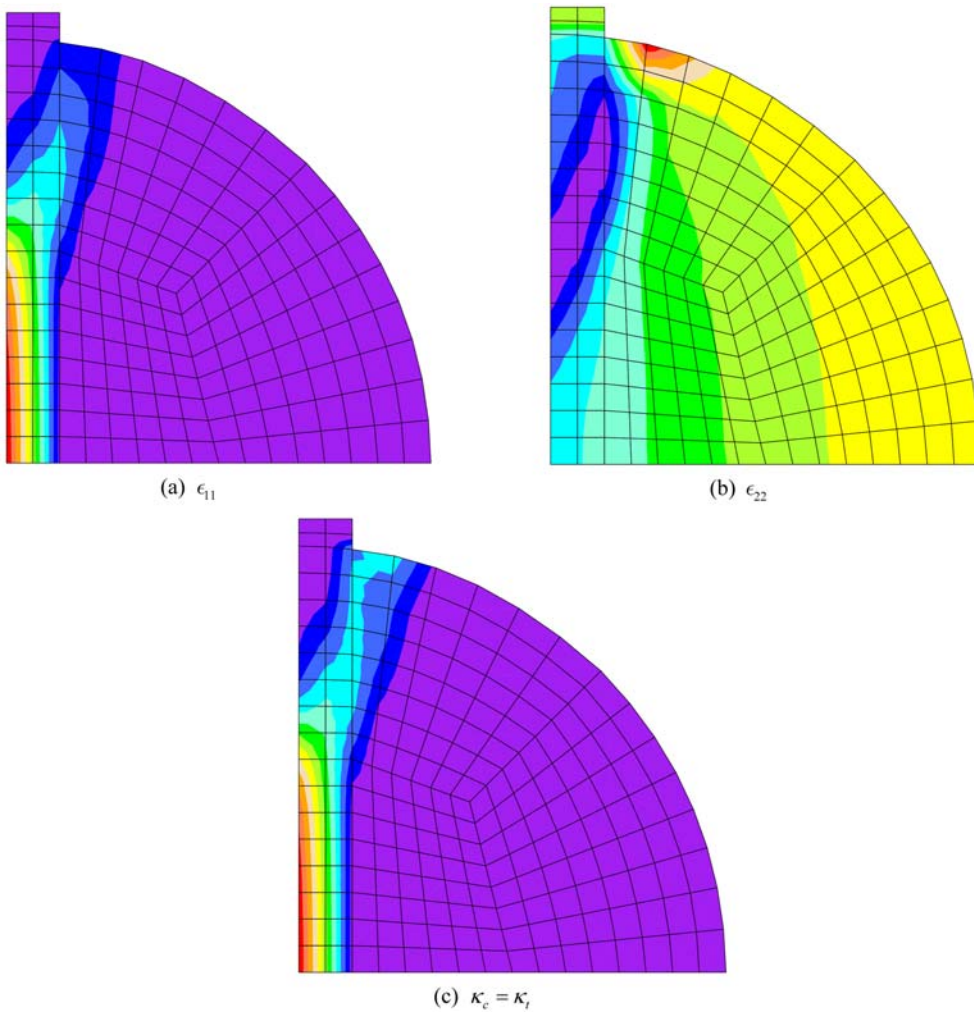


Fig. 16 Viscoplastic consistency, “isotropic” model, slow load rate, contour plots

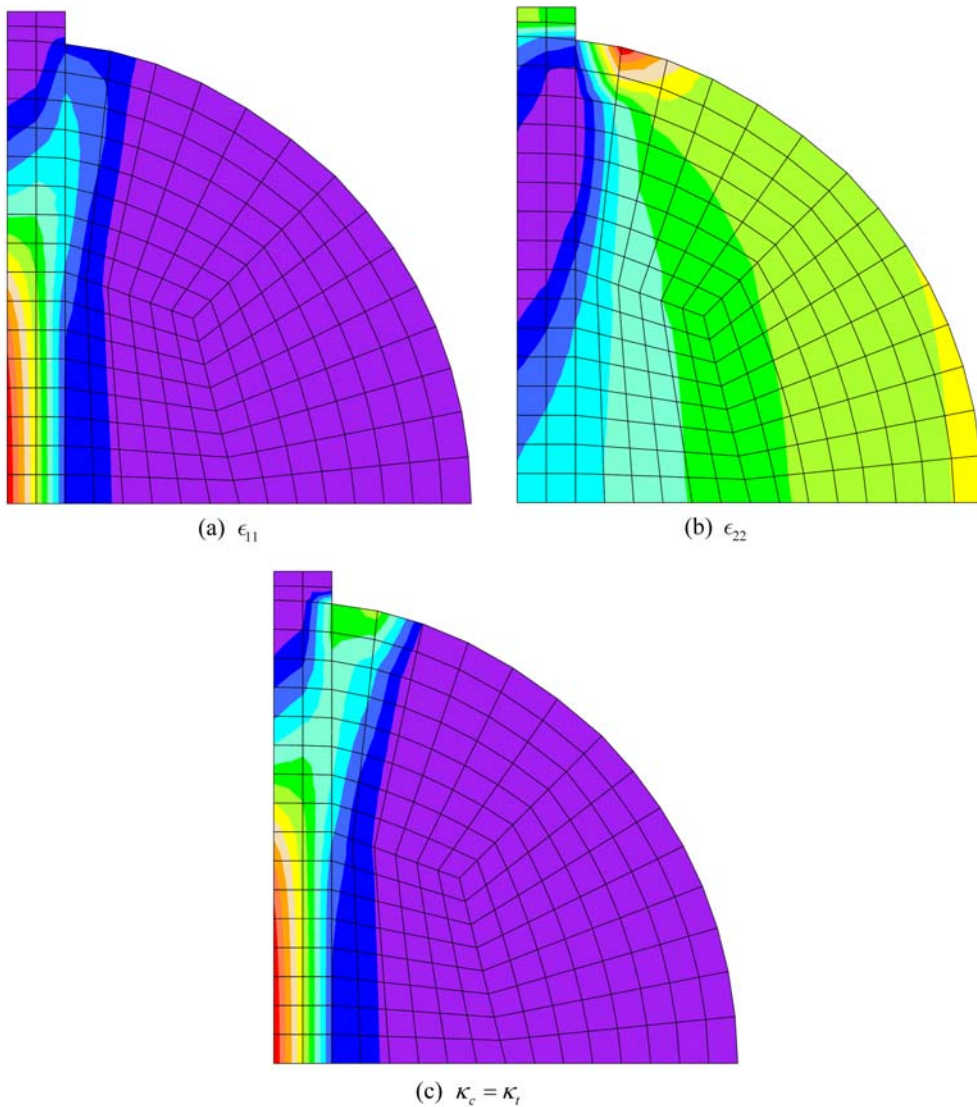


Fig. 17 Viscoplastic consistency, “isotropic” model, medium load rate, contour plots

strain  $\epsilon_{11}$ ). The concentration is induced just after the primary crack formation and it can depend on the value of the internal length parameter.

The internal length parameter which is incorporated in the averaging Eq. (12) decides in the Brazilian test whether or not and how the splitting phenomenon appears. The diagrams in Fig. 11 show that with a decreasing value of  $l$  the material becomes more brittle. All solutions are obtained for mesh M20. When the parameter equals 3 mm the splitting phenomenon does not occur. It is reflected in the contour plots (Fig. 12) and in the diagram with gradual softening. The loading path for  $l$  equal to 12 mm first exhibits a moderate softening stage and then a snapback drop, in contrast with the diagram for  $l = 6$  mm. The higher the value of  $l$ , the more delayed the snapback is. Moreover, if Figs. 9 and 12(d)-12(f) are confronted, it can be concluded that the localization zone

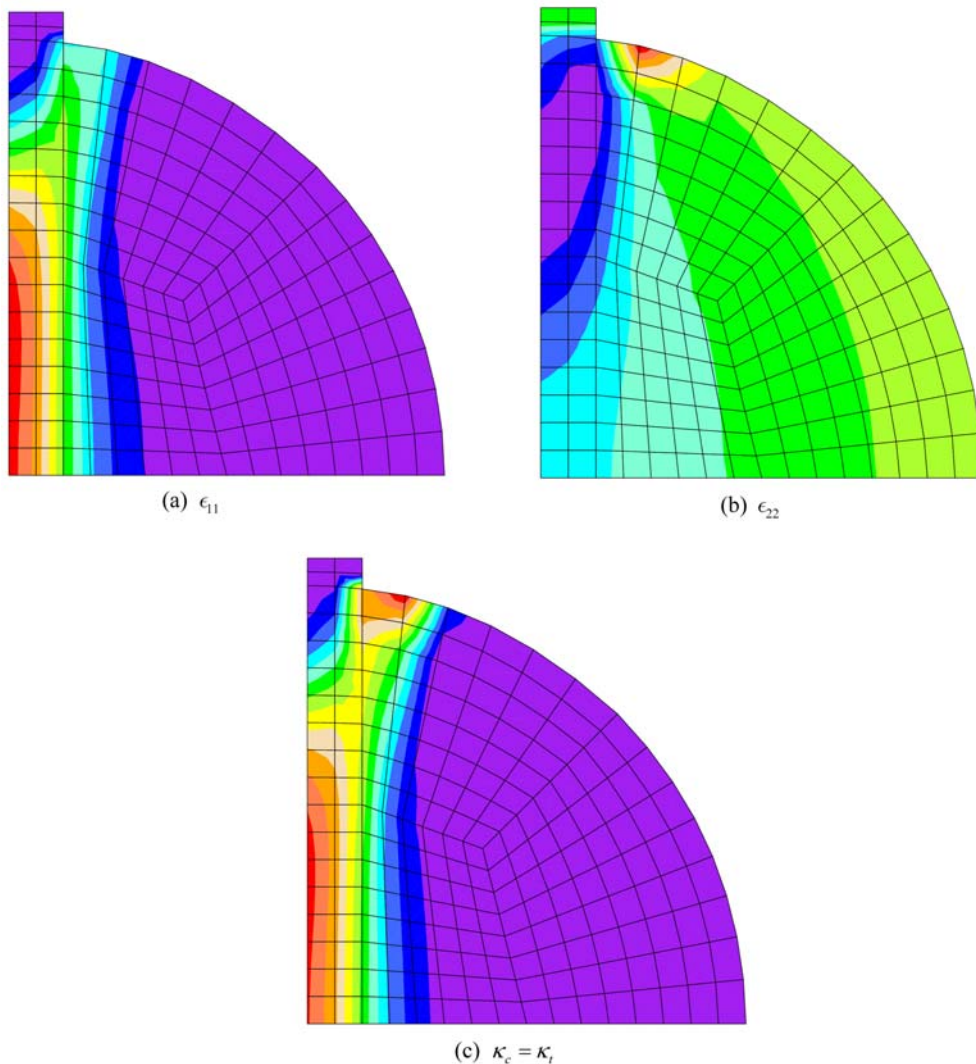


Fig. 18 Viscoplastic consistency, “isotropic” model, fast load rate, contour plots

broadens together with the increase of the internal length scale. In the last case ( $l = 12$  mm) the concentration of strains in the area under the platen almost vanishes, as is depicted in Fig. 12(d).

For mesh M20 we also examine the influence of ductility parameter  $\eta$ . The larger the value of this parameter is the smaller the value of fracture energy  $G_f$  is involved and the more brittle response is observed. The diagrams in Fig. 13 show that below a limit value of ductility parameter, which is between  $\eta = 600$  and  $\eta = 800$ , a snapback and the splitting effect occur. The deformations presented in Fig. 14 confirm the above observation. For cases  $\eta = 400$  and  $\eta = 600$  we can notice horizontal displacements along the vertical axis, which means that the split in the middle is simulated. On the contrary, for  $\eta = 800$  and  $\eta = 1200$ , when a more brittle material is assumed, we observe deformations concentrated directly below the bearing strip and no split is predicted.

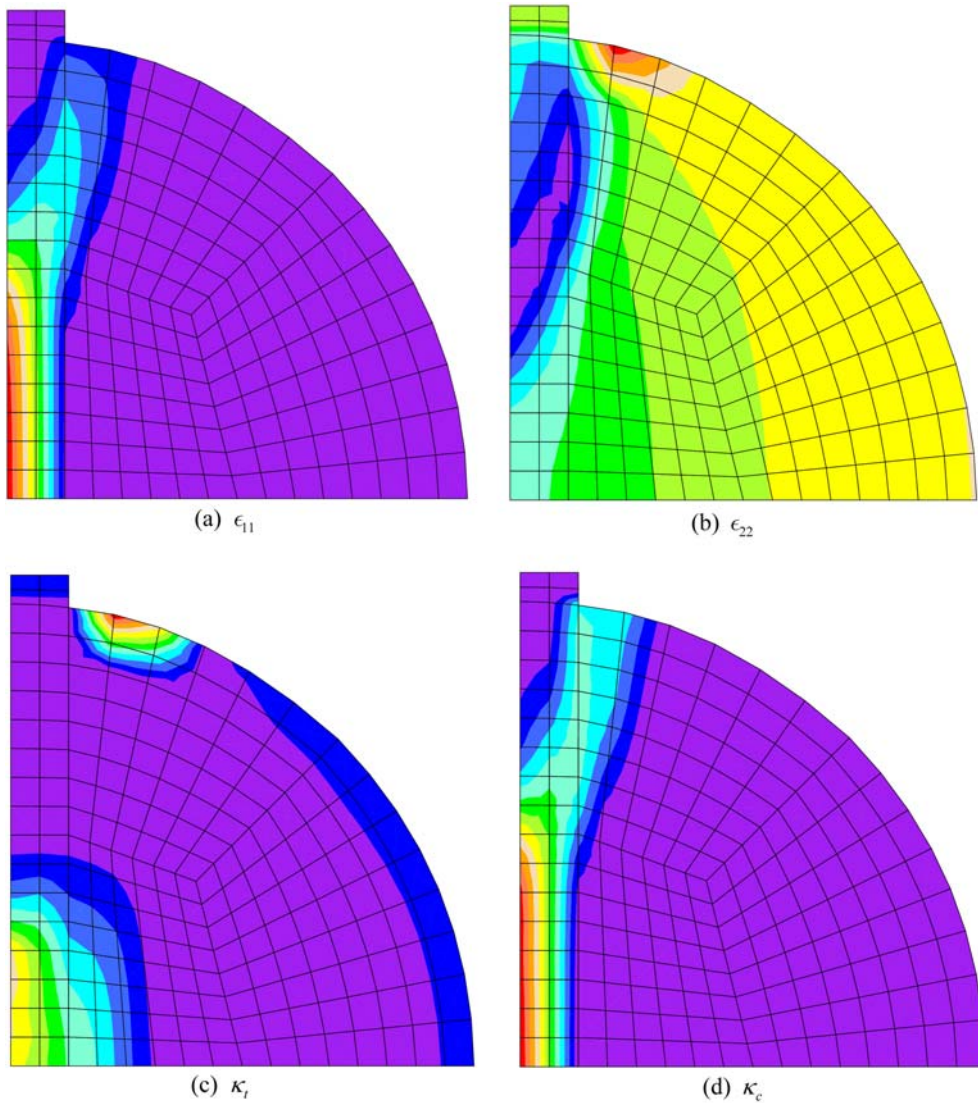


Fig. 19 Viscoplastic consistency, “nonisotropic” model, slow load rate, contour plots

### 5.2 Viscoplastic consistency model

All computations for the results presented in this subsection were performed using the four-noded coarse mesh. We do not consider mesh sensitivity, but we will show that viscoplasticity is an effective localization limiter, (see also e.g. Wang 1997). Firstly, Fig. 15 presents the structural response for different loading rates, also taking into account the relation between functions  $g_c$  and  $g_t$ , see Eqs. (36) and (37). In these cases the load is applied through the platen. Generally, load-displacement diagrams for the “nonisotropic” model ( $g_c \neq g_t$ ) exhibit slightly lower peak loads than for the “isotropic” model ( $g_c = g_t = 1$ ), but the softening intensity after the peak is quite similar. Additionally, the higher strain rates result in larger maximum loads and corresponding displacements. The

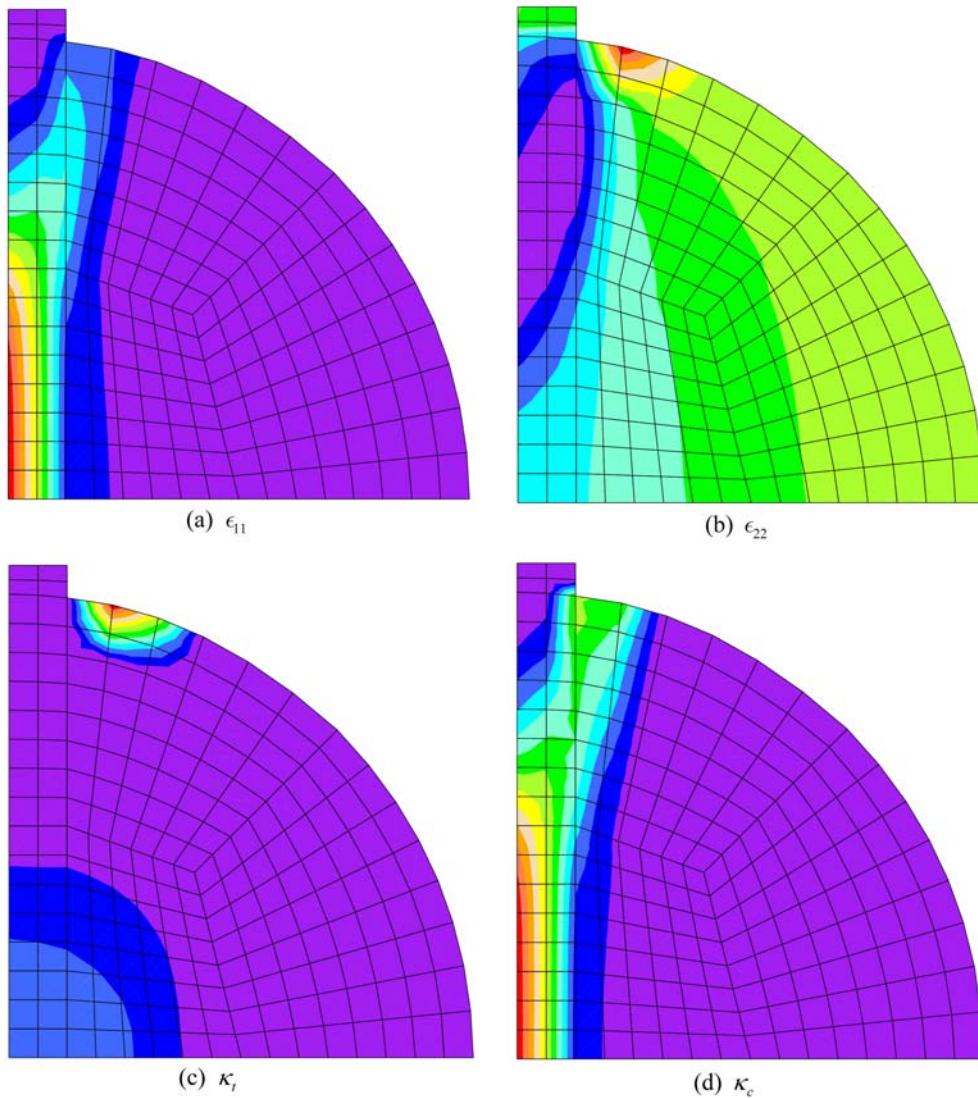


Fig. 20 Viscoplastic consistency, “nonisotropic” model, medium load rate, contour plots

postcritical part of the diagram is also less steep for a higher strain rate.

Figs. 16-21 present contour plots for both the total values of strain – horizontal component  $\epsilon_{11}$ , vertical component  $\epsilon_{22}$  and internal variables –  $\kappa_t$  and  $\kappa_c$  (which are equal for the “isotropic” model) at the end of the loading process. We observe that the horizontal component of strain is highly localised. Damage is localised in the narrow vertical zone in the middle of the specimen, forming a wedge at the top under the platen. For higher strain rates the width of the localisation zone becomes larger, which proves that the rate-dependence plays the role of localization limiter.

When the internal parameters  $\kappa_t$  and  $\kappa_c$  are different in the “nonisotropic” model, it is visible that damage in compression (variable  $\kappa_c$ ) at the end of loading process is more localised along the vertical symmetry axis than damage in tension (variable  $\kappa_t$ ), cf. for example Figs. 21(c) and 21(d). It

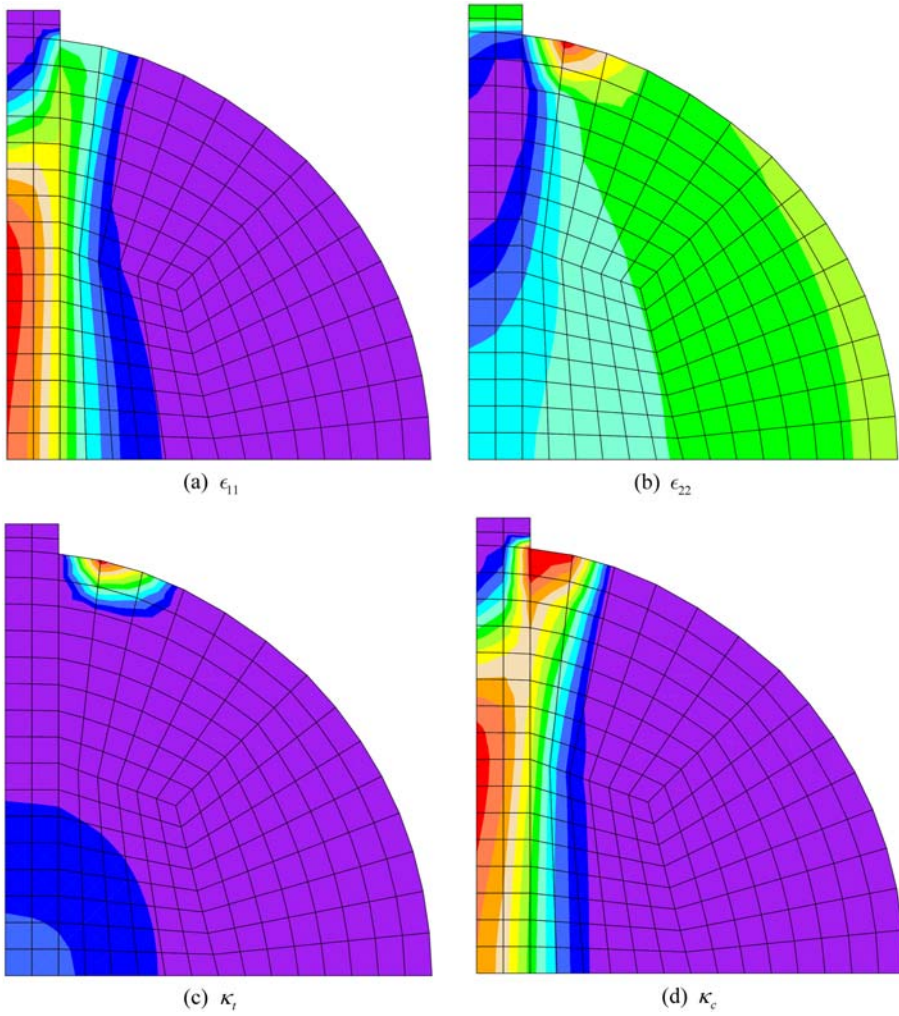


Fig. 21 Viscoplastic consistency, “nonisotropic” model, fast load rate, contour plots

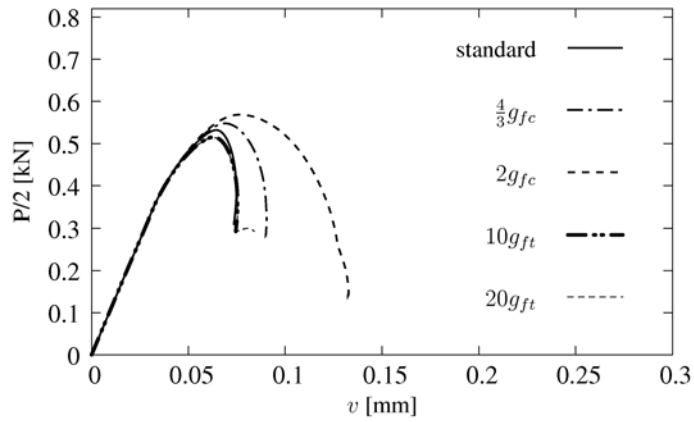


Fig. 22 Viscoplastic consistency, influence of applied functions  $H_c$  and  $H_b$ , diagrams

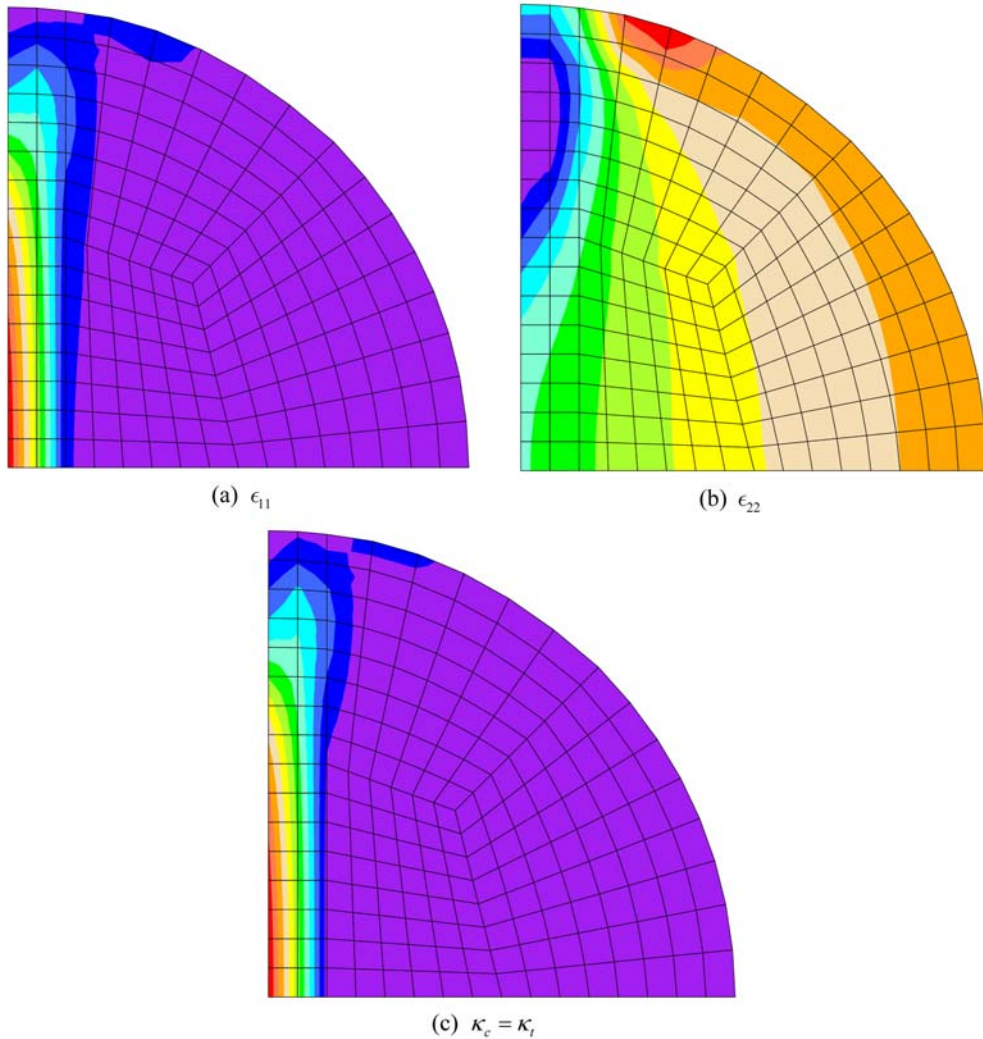


Fig. 23 Viscoplastic consistency, standard case:  $g_{fc} = 225.0$  kPa,  $g_{ft} = 1.50$  kPa, contour plots

seems surprising that the failure mechanism is connected with damage development in compression and not in tension. This finding will be also confirmed in next paragraphs.

Now we show the results of computations, where the specimen is loaded without the platen. The question whether the incorporation of the platen in the numerical model is necessary will be discussed in the next section. However, we can point out here that the existence of the platen does not change the results substantially. We also introduce  $S_t = S_c \equiv 1$ , remembering that the localisation zone then coincides with one row of finite elements and focusing our attention on the definition of material functions  $H_c$  and  $H_t$ . In the load-displacement diagrams in Fig. 22 we notice that different definitions of  $H_t$  have a negligibly small influence on the loading path. On the other hand, the postcritical behaviour at the structural level depends on the assumed ductility in compression.

In Figs. 23-27 we depict the contour plots for the total values of strain (horizontal component  $\epsilon_{11}$ , vertical component  $\epsilon_{22}$ ) and internal variables  $\kappa_t = \kappa_e$ . Both the total strain and internal parameters

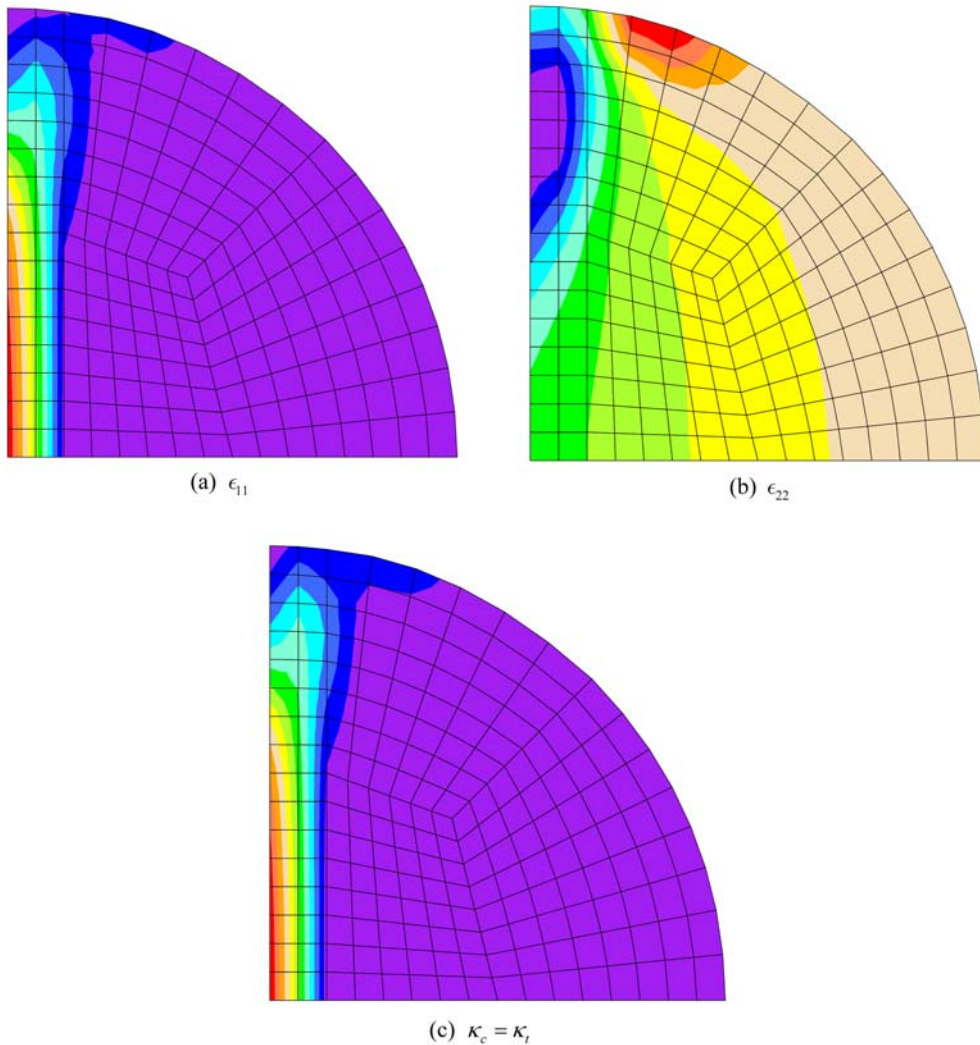


Fig. 24 Viscoplastic consistency, case with  $\frac{4}{3}g_{fc}$  (300.0 kPa) and  $g_{ft}=1.50$  kPa, contour plots

represent highly localised damage in the form of a narrow vertical zone near the symmetry axis. This is in agreement with the experimentally observed mechanism of failure. We can also see that a wedge forms under the loaded area, which also compares well with experiments. A larger value of the fracture energy in compression  $g_{fc}$  (cf. Fig. 25) results in a more pronounced damage zone at the top of the specimen. On the other hand, the change in the value of  $g_{ft}$  has practically no influence on the obtained patterns (see e.g. Fig. 27) in comparison to the standard case (Fig. 23). Hence, the contour plots confirm that different definitions of  $H_c$  influence the concrete behaviour simulated in this test, whereas the change of  $H_t$  does not.

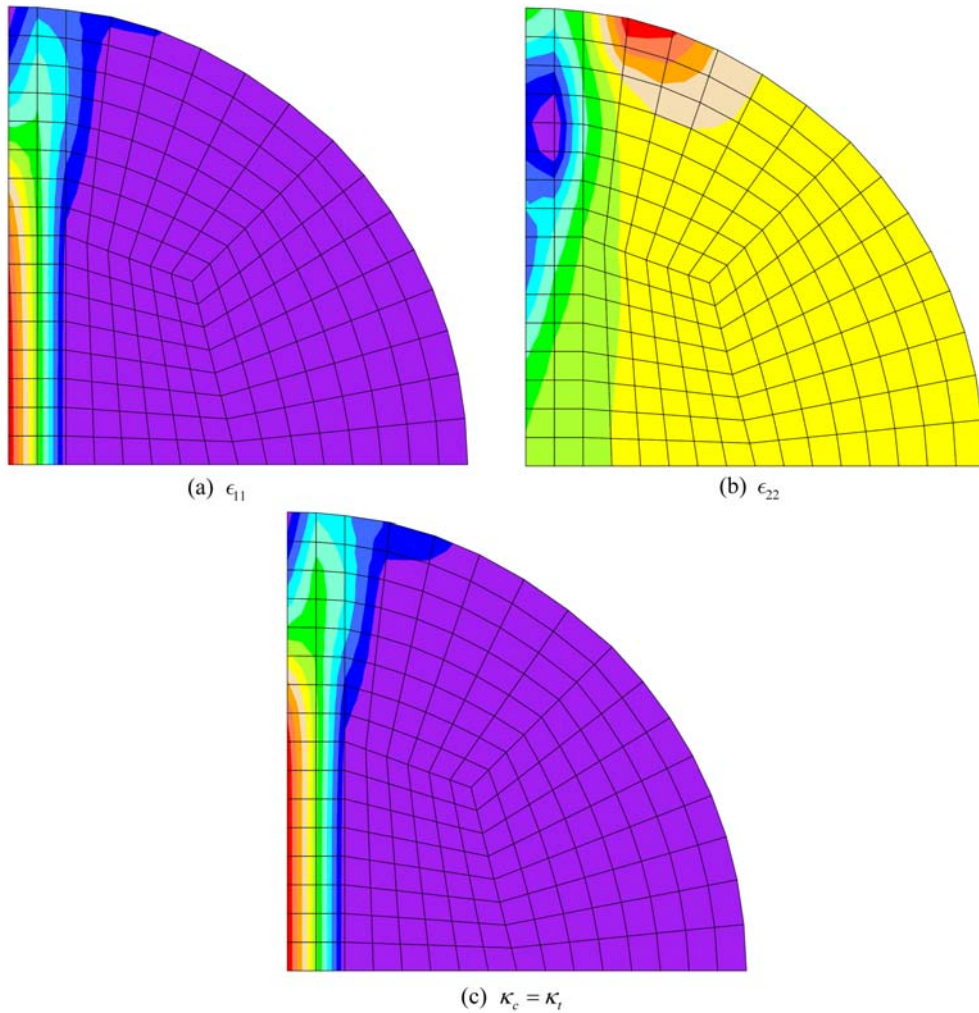


Fig. 25 Viscoplastic consistency, case with  $2g_c$  (450.0 kPa) and  $g_{fi} = 1.50$  kPa, contour plots

### 5.3 Comparison of models

In Figs. 28 and 29 we compare load-displacement diagrams for the two considered numerical models and additionally different platen representations. The data for gradient damage are shown in Tables 1 and 2. Tables 1 and 4 summarize the data for the viscoplastic consistency model, material curves  $H_c$  and  $H_t$  are like for the standard case from Figs. 6(a) and 6(b). We also assume  $S_t = S_c \equiv 1$ . The diagrams for the coarse mesh with four-noded elements, which corresponds to mesh C12 (see Table 3 and Fig. 5(a)), are depicted in Fig. 28. To confront these results, we also perform computations for eight-noded medium mesh, which corresponds to mesh M20 (see Table 3 and Fig. 5(b)). The loading paths for this mesh are presented in Fig. 29.

Considering the presence of the platen in the numerical model, the load-displacement paths run very closely to each other, although the cases without the platen exhibit a slightly smaller initial

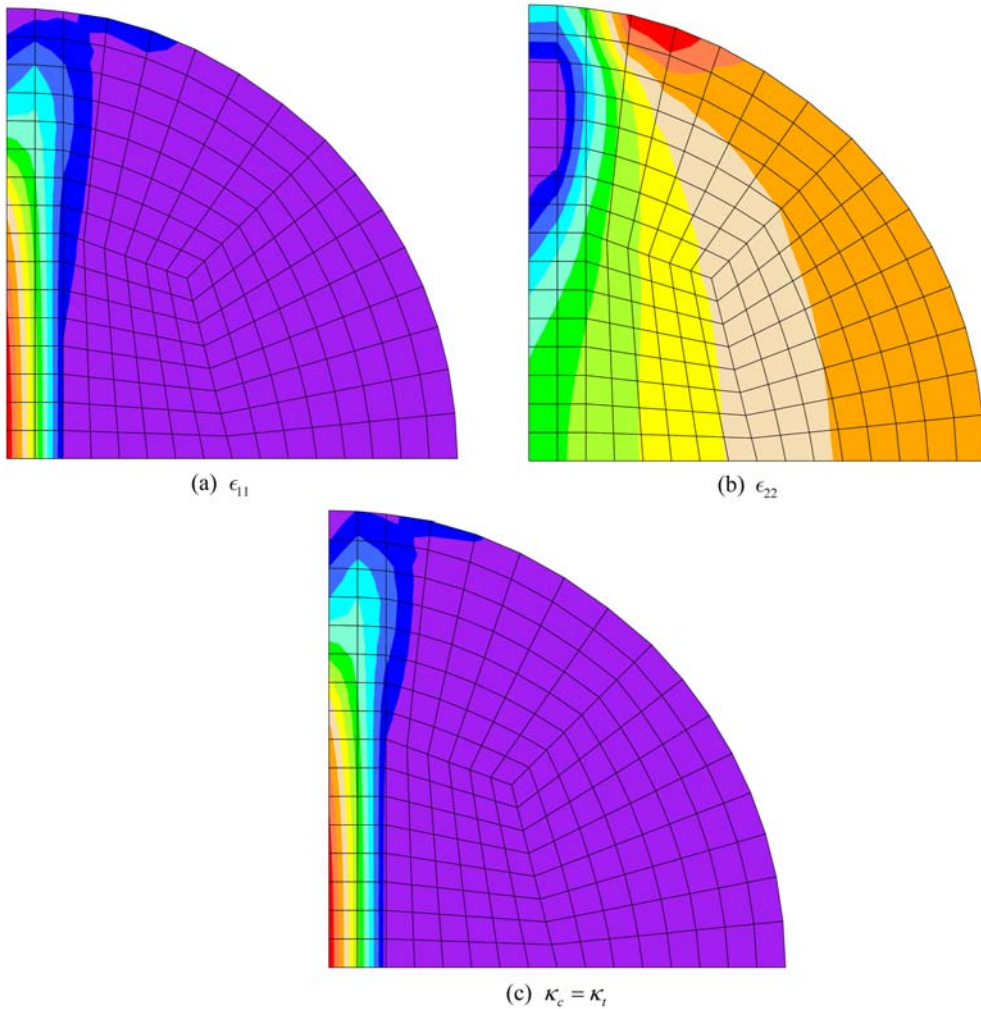


Fig. 26 Viscoplastic consistency, case with  $g_{fc} = 225.0$  kPa, and  $10g_{ft}$  (15.0 kPa), contour plots

stiffness and less pronounced snapback. For gradient damage we obtain snapback response after a similar peak load level and then a slow convergence to the same residual load level, while for Burzyński-Hoffman viscoplasticity the loading paths reach the peak point, drop until the snapback effect and finally computations diverge at some load level, even though the consistent tangent matrix was used (details of the consistent tangent matrix formulation are given in Winnicki 2007). We notice that the carrying capacity is about 20 per cent larger for viscoplastic consistency in comparison to gradient damage.

The contour plots in Figs. 30 and 31 are produced for the gradient damage model and the configuration without the platen. If we confront them with contour plots shown in Figs. 8 and 9 we can notice that the incorporation of the platen is insignificant.

A similar observation is made for Burzyński-Hoffman viscoplasticity, although here when the platen is considered the wedge formation is slightly more clear (compare Fig. 23 with Fig. 32 and Fig. 33 with Fig. 34).

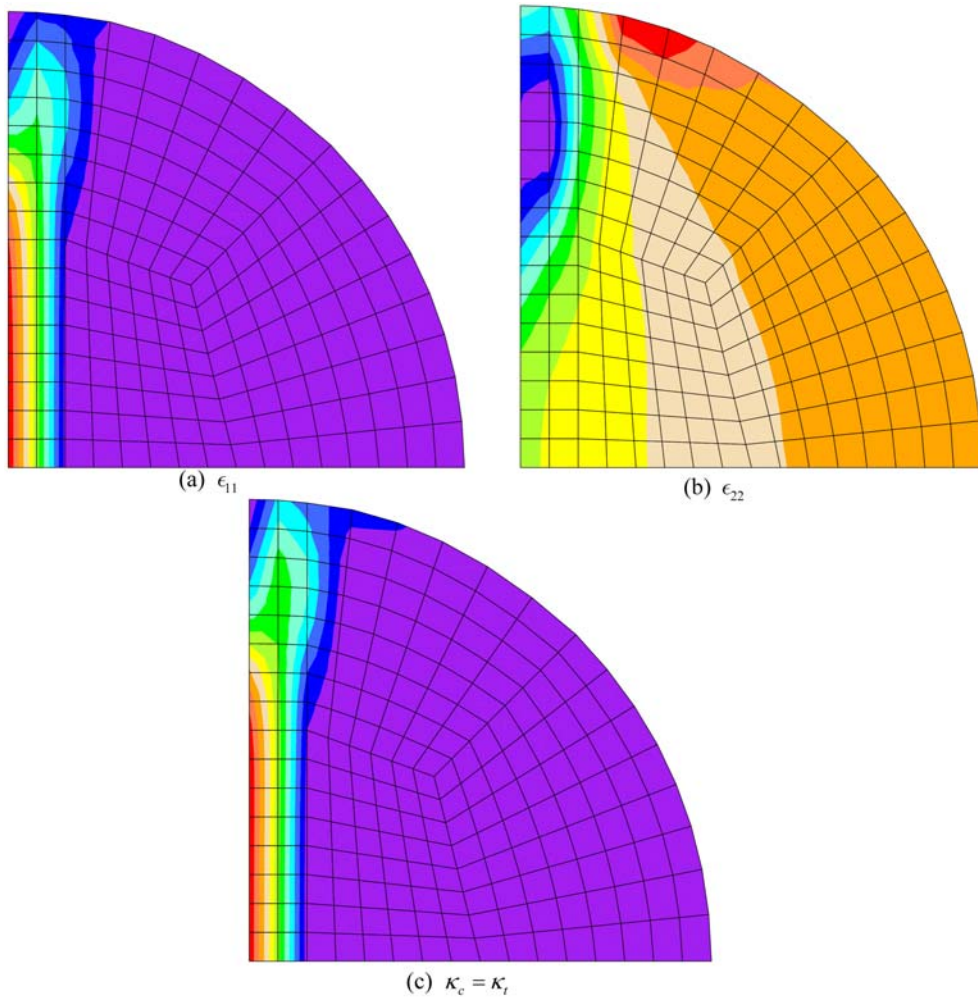


Fig. 27 Viscoplastic consistency, case with  $g_{fc} = 225.0$  kPa, and  $20g_{ft}$  (30.3 kPa), contour plots

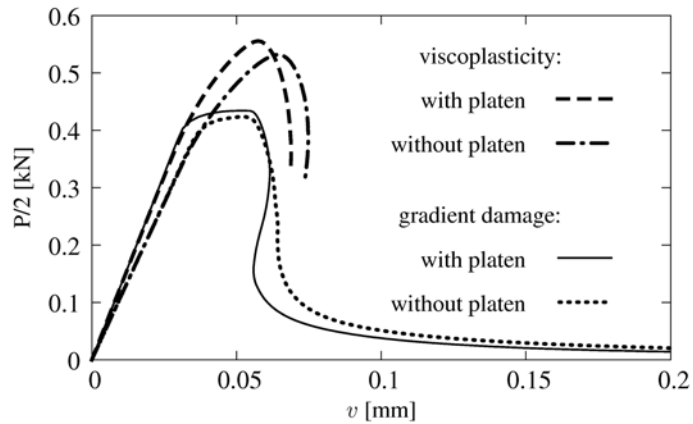


Fig. 28 Comparison of models, results for four-noded coarse mesh (C12), diagrams

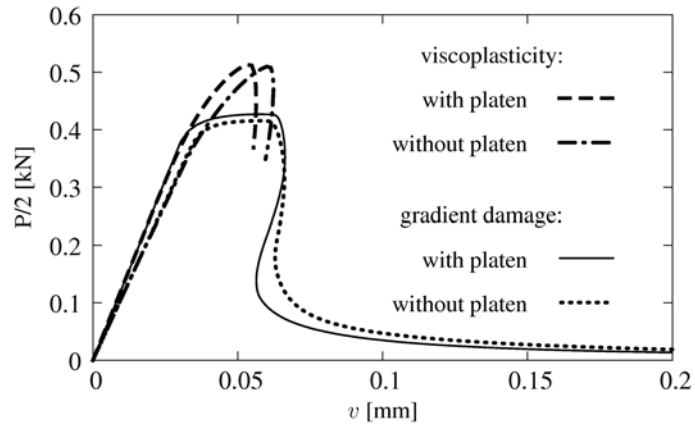


Fig. 29 Comparison of models, results for eight-noded medium mesh (M20), diagrams

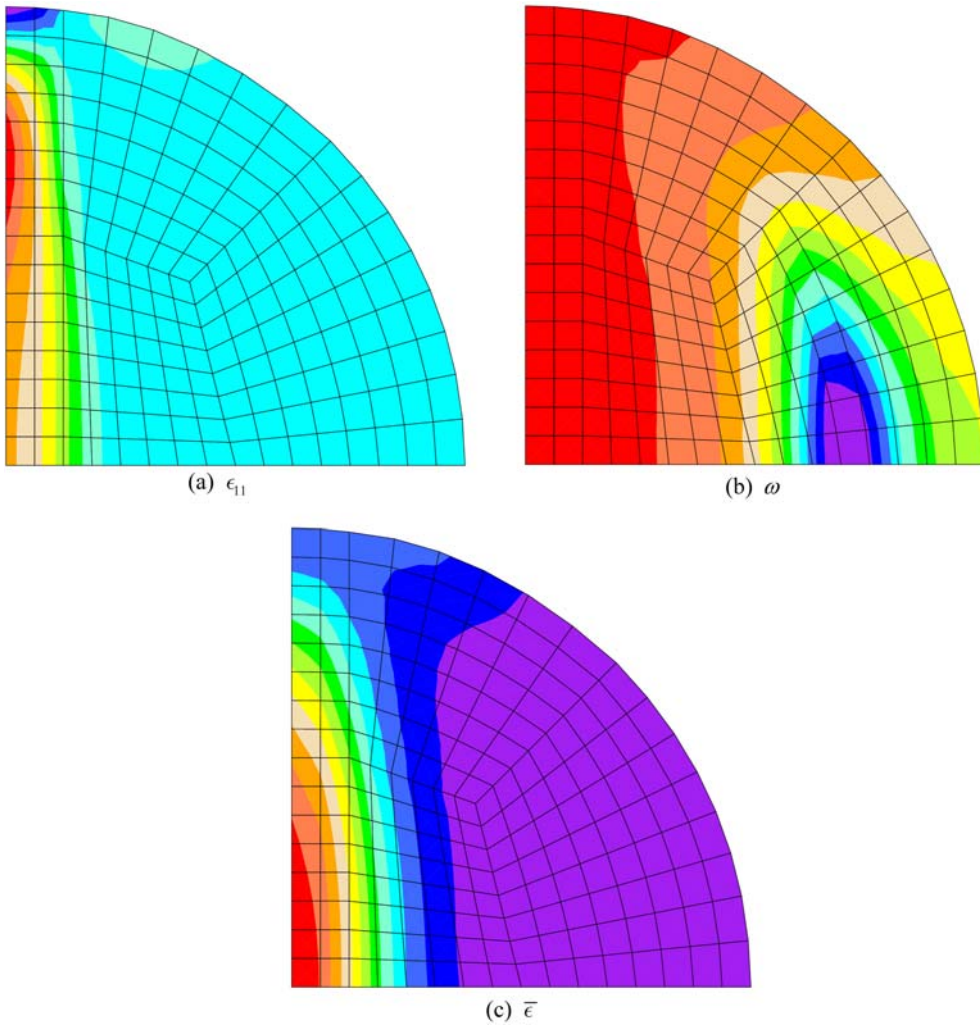


Fig. 30 Gradient damage, contour plots for mesh C12wp without platen

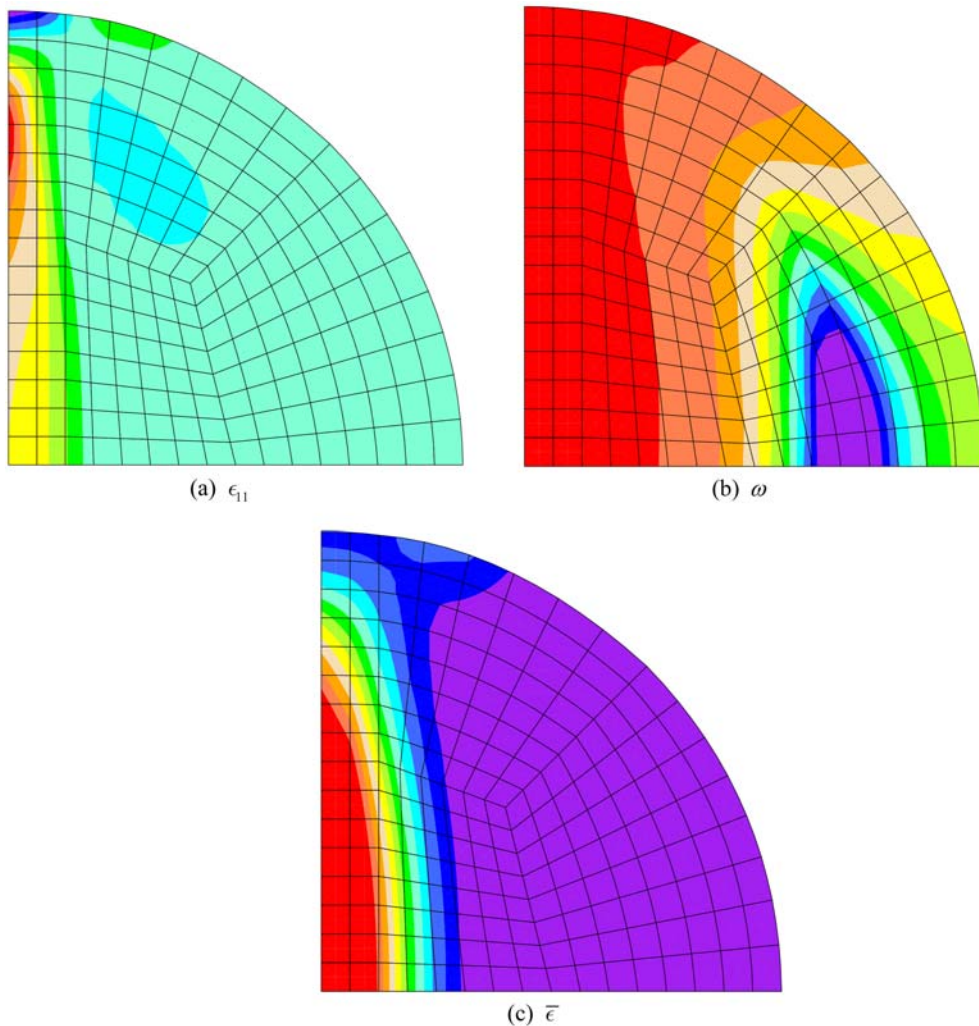


Fig. 31 Gradient damage, contour plots for mesh M20wp without platen

The character of the splitting process is analogical for the two models, however the final localization patterns are different for each of them. We can see the primary crack formation near the vertical symmetry axis, but for the viscoplastic consistency model the wedge also occurs. The simulated crack patterns for both models are comparable to those observed in experiments, although no secondary cracks are predicted by either of the models. For the gradient damage model the strong damage zone expansion which is a feature of the model with constant parameter  $c$  prevents stress build-up at a distance from the primary crack, required to initiate another crack. For the Hoffman viscoplasticity model the localization zone is much narrower, but the wedge pattern predicted excludes an alternative pattern with two parallel cracks.

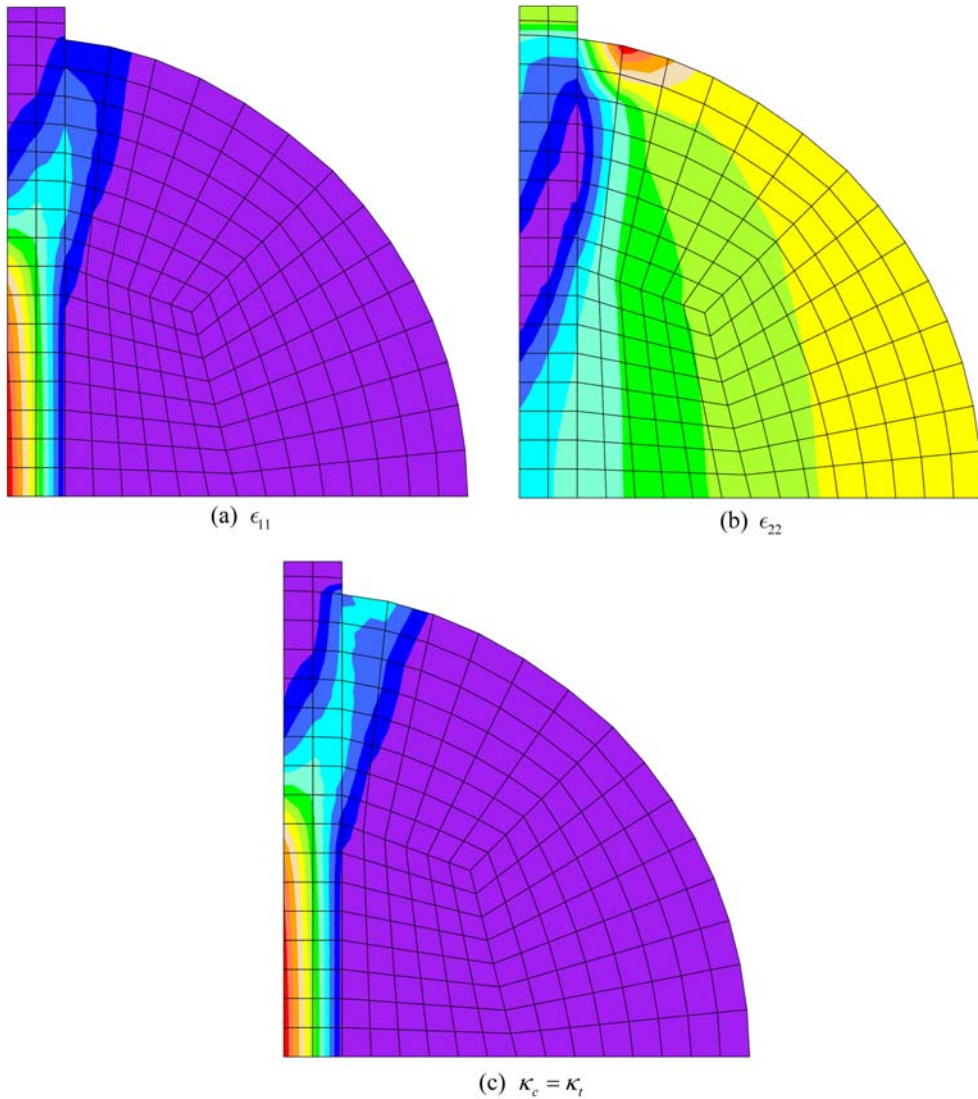


Fig. 32 Viscoplastic consistency, contour plots for four-noded coarse mesh with platen

## 6. Conclusions

Different aspects of numerical simulation of the Brazilian split test have been analyzed using two material models equipped with localization limiters. Realistic simulation results have been obtained: larger internal length and loading rate result in higher peak load and model ductility.

For the gradient damage model the discretization insensitivity has been demonstrated, the influence of the internal length and the ductility parameter in the damage growth function have been analyzed. It has been observed that for a low value of internal length and fracture energy no split is observed and the damage localizes directly under the platen.

For the viscoplastic consistency model the regularization effect has also been shown. The strain

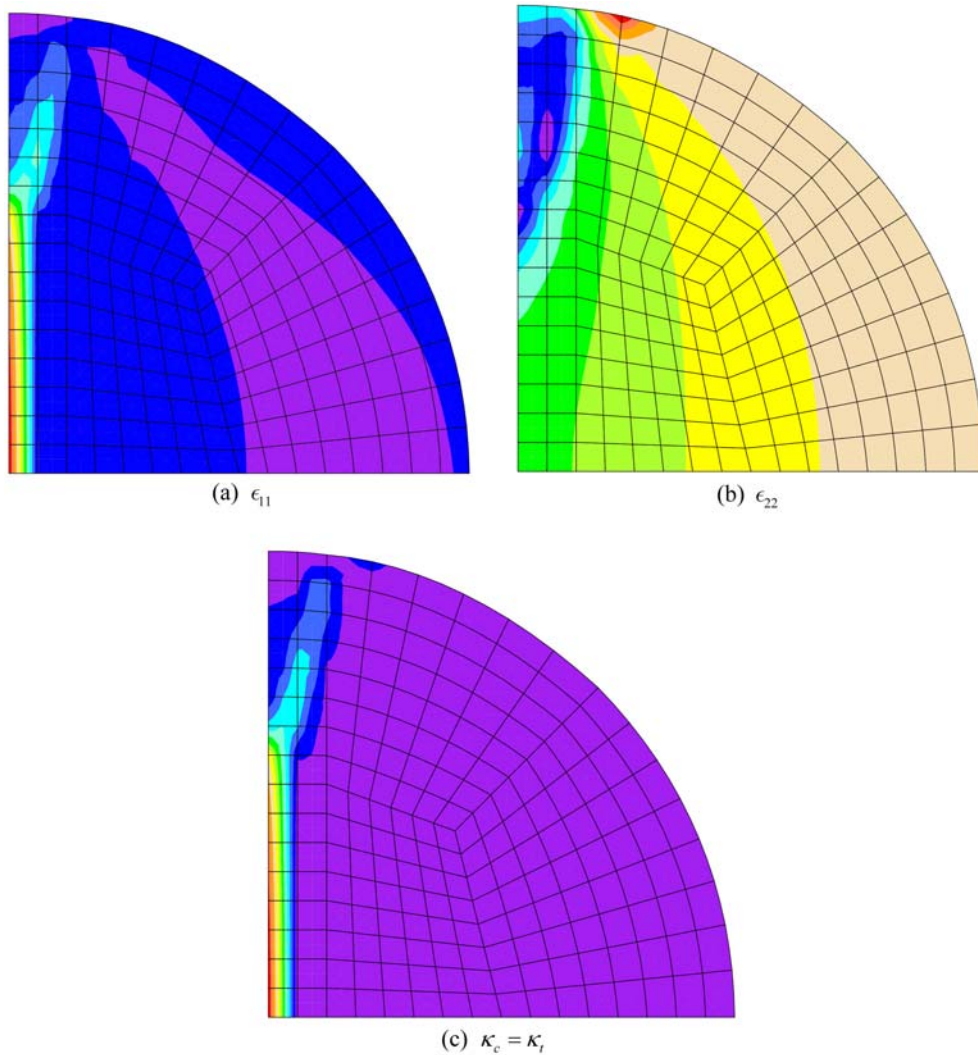


Fig. 33 Viscoplastic consistency, contour plots for eight-noded medium mesh without platen

rate sensitivity has been examined for two versions of the model: with one internal variable for compression and tension or independent ones for the two stress states. It has turned out that the response is strongly sensitive to the assumed material ductility in compression.

Both models are capable of representing different behaviour in tension and compression. For the viscoplastic Hoffman model it is possible to link the model behaviour in tension and compression directly with experiments. To achieve this in the damage model its isotropic (and not scalar) version with two damage parameters degrading independently the tensile and compressive stiffnesses (cf. Mazars and Pijaudier-Cabot 1989, Comi 2001) would have to be considered.

Finally, in Section 5.3 a comparison of the response provided by the two constitutive models is shown for the models with and without the loading platen, the influence of which on the results is minor. It is noticed that a different localized strain distribution is simulated by the models, especially in the zone under the applied load: the gradient model predicts a vertical damage zone

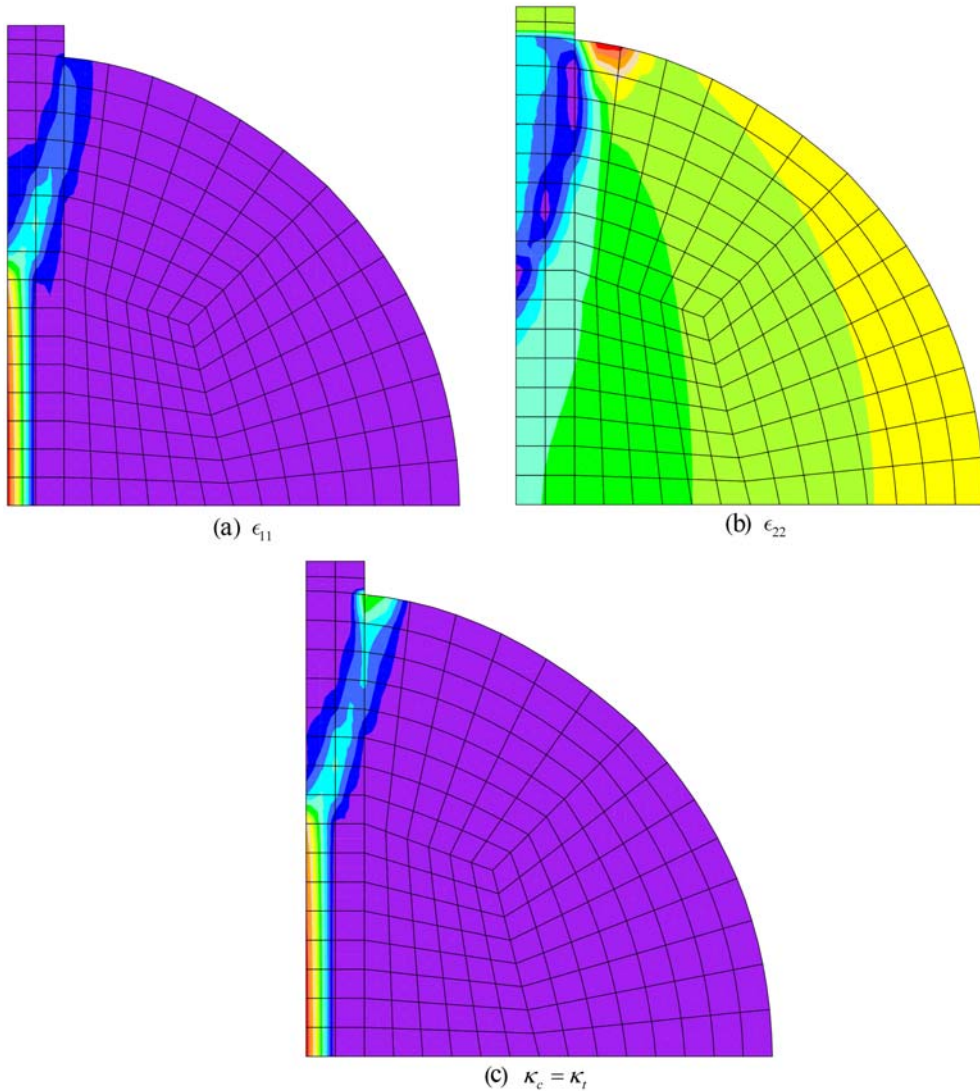


Fig. 34 Viscoplastic consistency, contour plots for eight-noded medium mesh with platen

under the platen (its width is determined by the internal length) while the viscoplastic model reproduces a band of localized equivalent strain in the centre of the specimen, which further inclines to form a wedge next to the load application area. No secondary cracks are simulated.

## References

- Askes, H., Pamin, J., and de Borst, R. (2000), "Dispersion analysis and element-free Galerkin solutions of second- and fourth-order gradient-enhanced damage models", *Int. J. Numer. Meth. Eng.*, **49**, 811-832.
- Bićanić, N., Pearce, C.J. and Owen, D.R.J. (1994), "Failure predictions of concrete like materials using softening Hoffman plasticity model", In Mang, H., Bićanić, N., and de Borst, R., editors, *Computational modelling of*

- concrete structures, *Euro-C 1994*, volume 1, pages 185-198, Swansea, UK. Pineridge Press.
- Chen, W.F. and Chang, T.Y.P. (1978), "Plasticity solutions for concrete splitting tests", *J. Eng. Mech. Div. - ASCE*, **104**(EM3), 691-704.
- Comi, C. (2001), "A non-local model with tension and compression damage mechanisms", *Eur. J. Mech. A - Solids*, **20**(1), 1-22.
- de Borst, R., Pamin, J. and Geers, M.G.D. (1999), "On coupled gradient-dependent plasticity and damage theories with a view to localization analysis", *Eur. J. Mech. A - Solids*, **18**(6), 939-962.
- de Vree, J.H.P., Brekelmans, W.A.M. and van Gils, M.A.J. (1995), "Comparison of nonlocal approaches in continuum damage mechanics", *Comput. Struct.*, **55**(4), 581-588.
- Feenstra, P.H. (1993), *Computational aspects of biaxial stress in plain and reinforced concrete*, Ph.D. dissertation, Delft University of Technology, Delft.
- fib (1999), *Structural concrete. The textbook on behaviour, design and performance*, Updated knowledge of the CEB/FIP Model Code 1990, volume 1, Bulletin No 1. fib.
- Geers, M.G.D. (1997), *Experimental analysis and computational modelling of damage and fracture*, Ph.D. dissertation, Eindhoven University of Technology, Eindhoven.
- Heeres, O.M., Suiker, A.S.J. and de Borst, R. (2002), "A comparison between the Perzyna viscoplastic model and the Consistency viscoplastic model", *Eur. J. Mech. A - Solids*, **21**, 1-12.
- Kachanov, L.M. (1958), "Time of rupture process under creep conditions", *Izd. Akad. Nauk SSSR, Otd. Tekh. Nauk*, **8**, 26-31. (in Russian)
- Kleiber, M. (1998), "Plasticity problems", Kleiber, M., editor, *Handbook of Computational Mechanics, Survey and Comparison of Contemporary Methods*, pages 201-252, Berlin, Germany, Springer Verlag.
- Kupfer, H. (1973), *Das Verhalten des Betons unter mehrachsiger Kurzzeitbelastung unter besonderer Berücksichtigung der zweiachsigen Beanspruchung*, Heft 229, Deutscher Ausschuss für Stahlbeton, Berlin.
- Lemaitre, J. (1971), "Evaluation of dissipation and damage in metals", *Proc. I.C.M.*, volume 1, Kyoto, Japan.
- Lopez, C.M., Carol, I. and Aguado, A. (2008), "Meso-structural study of concrete fracture using interface elements. II: Compression, biaxial and Brazilian test", *Mater. Struct.*, **41**, 601-620.
- Mazars, J. and Pijaudier-Cabot, G. (1989), "Continuum damage theory - application to concrete", *J. Eng. Mech. - ASCE*, **115**, 345-365.
- Pamin, J., Wosalko, A. and Winnicki, A. (2003), "Two- and three-dimensional gradient damage-plasticity simulations of cracking in concrete", In Bićanić, N. et al., editors, *Proc. EURO-C 2003 Int. Conf. Computational Modelling of Concrete Structures*, pages 325-334, Rotterdam/Brookfield. A.A. Balkema.
- Pearce, C.J. (1993), *Computational aspects of the softening Hoffman plasticity model for quasi-brittle solids*, M.Sc., University Of Wales, College Swansea.
- Peerlings, R.H.J., de Borst, R., Brekelmans, W.A.M. and de Vree, J.H.P. (1996), "Gradient-enhanced damage for quasi-brittle materials", *Int. J. Numer. Meth. Eng.*, **39**, 3391-3403.
- Peerlings, R.H.J., de Borst, R., Brekelmans, W.A.M. and Geers, M.G.D. (1998), "Gradient-enhanced damage modelling of concrete fracture", *Mech. Cohes.-frict. Mater.*, **3**, 323-342.
- Perzyna, P. (1966), "Fundamental problems in viscoplasticity", *Recent Advances in Applied Mechanics*, volume 9, pages 243-377, New York, USA. Academic Press.
- Reinhardt, H.W. (1984), "Fracture mechanics of an elastic softening material like concrete", *Heron*, **29**(2).
- Rocco, C., Guinea, G.V., Planas, J. and Elices, M. (1999), "Mechanisms of rupture in splitting tests", *ACI Mater. J.*, **96**, 52-60.
- Rocco, C., Guinea, G.V., Planas, J. and Elices, M. (2001), "Review of the splitting-test standards from a fracture mechanics point of view", *Cement Concrete Res.*, **31**, 73-82.
- Rodriguez-Ferran, A. and Huerta, A. (2001), "Failure and post-failure modelling of the Brazilian test", Bletzinger, K.U., Schweizerhof, K. and Wall, W., editors, *Conf. on Trends in Computational Structural Mechanics*, pages 189-197, Barcelona, CIMNE.
- Ruiz, G., Ortiz, M. and Pandolfi, A. (2000), "Three-dimensional finite-element simulation of the dynamic Brazilian tests on concrete cylinders", *Int. J. Numer. Meth. Eng.*, **48**, 963-994.
- Simo, J.C. and Hughes, T.J.R. (1997), *Computational inelasticity*, Springer Verlag, New York, Berlin.
- Simo, J.C. and Ju, J.W. (1987), "Strain- and stress-based continuum damage models - I. Formulation, II. Computational aspects", *Int. J. Solids Struct.*, **23**(7), 821-869.

- Suaris, W. and Shah, S.P. (1985), "Constitutive model for dynamic loading of concrete", *J. Struct. Eng. - ASCE*, **111**(3), 563-576.
- Taylor, R.L. (2001), *FEAP - A finite element analysis program*, Version 7.4, User manual, Technical report, University of California at Berkeley, Berkeley.
- van Mier, J.G.M. (1984), *Strain-softening of concrete under multiaxial loading conditions*, Ph.D. dissertation, Eindhoven University of Technology, Eindhoven.
- Vonk, R.A. (1992), *Softening of concrete loaded in compression*, Ph.D. dissertation, Eindhoven University of Technology, Eindhoven.
- Wang, W.M. (1997), *Stationary and propagative instabilities in metals - a computational point of view*, Ph.D. dissertation, Delft University of Technology, Delft.
- Winnicki, A. (2001), "Viscoplastic consistency model - basic features", Waszczyszyn, Z. and Pamin, J., editors, *European Conf. on Computational Mechanics ECCM-2001*, Cracow, Cracow University of Technology.
- Winnicki, A. (2007), *Viscoplastic and internal discontinuity models in analysis of structural concrete*, Series Civil Engineering, Monograph 349, Cracow University of Technology, Cracow.
- Winnicki, A., Pearce, C.J. and Bićanić, N. (2001), Viscoplastic Hoffman consistency model for concrete, *Comput. Struct.*, **79**, 7-19.
- Życzkowski, M. (1981), *Combined loadings in the theory of plasticity*, PWN - Polish Scientific Publishers, Warszawa.